DOT/FAA/TC-15/51

Federal Aviation Administration
William J. Hughes Technical Center
Aviation Research Division
Atlantic City International Airport
New Jersey 08405

Composite Thermal Damage Measurement With Handheld Fourier Transform Infrared Spectroscopy

January 2017

Final Report

This document is available to the U.S. public through the National Technical Information Services (NTIS), Springfield, Virginia 22161.

This document is also available from the Federal Aviation Administration William J. Hughes Technical Center at actlibrary.tc.faa.gov.

U.S. Department of Transportation
Federal Aviation Administration

NOTICE

This document is disseminated under the sponsorship of the U.S. Department of Transportation in the interest of information exchange. The U.S. Government assumes no liability for the contents or use thereof. The U.S. Government does not endorse products or manufacturers. Trade or manufacturers' names appear herein solely because they are considered essential to the objective of this report. The findings and conclusions in this report are those of the author(s) and do not necessarily represent the views of the funding agency. This document does not constitute FAA policy. Consult the FAA sponsoring organization listed on the Technical Documentation page as to its use.

This report is available at the Federal Aviation Administration William J. Hughes Technical Center's Full-Text Technical Reports page: actlibrary.tc.faa.gov in Adobe Acrobat portable document format (PDF).

Technical Report Documentation Page

1. Report No.	2. Government Accession No.	3. Recipient's Catalog No.
DOT/FAA/TC-15/51		

4. Title and Subtitle	5. Report Date
COMPOSITE THERMAL DAMAGE MEASUREMENT WITH HANDHELD FOURIER TRANSFORM INFRARED SPECTROSCOPY	January 2017
	6. Performing Organization Code
7. Author(s)	8. Performing Organization Report No.
Tucker Howie, Ashley Tracey, Brian Flinn	
9. Performing Organization Name and Address	10. Work Unit No. (TRAIS)
University of Washington Materials Science and Engineering Department 302 Roberts Hall, Box 352120 Seattle, WA 98195-2120	11. Contract or Grant No.
12. Sponsoring Agency Name and Address	13. Type of Report and Period Covered
U.S. Department of Transportation Federal Aviation Administration 950 L'Enfant Plaza North, S.W. Washington, DC 20024	Final Report
	14. Sponsoring Agency Code
	AFS-300

15. Supplementary Notes

The Federal Aviation Administration William J. Hughes Technical Center Aviation Research Division COR was David Westlund.

16. Abstract

Incipient thermal damage (ITD) of carbon fiber-reinforced plastic (CFRP) composites cannot be detected by common nondestructive evaluation (NDE) methods such as ultrasound or visual inspection. ITD, however, can reduce matrix-dominated mechanical properties of composites and therefore requires detection and evaluation to ensure the integrity of composite structures that may be subjected to thermal exposures. Fourier transform infrared (FTIR) spectroscopy is an established technique that has shown promise for NDE of ITD. The purpose of this work was to investigate using FTIR to guide inspection and repair of panels with ITD.

The first step in the process was to take FTIR measurements on uniformly heated composite samples with various levels of ITD and correlate the spectra to short-beam strength measurements from those samples using a partial least squares (PLS) model. FTIR inspections for ITD were then performed on CFRP panels with various levels of localized thermal exposure using the PLS models to predict the strength (damage) at points spaced 1.27 cm (0.5″) apart. Localized heating was created using a heat blanket coupled with multiple layers of insulation in the center of the panels. The panels inspected were held for 1 hour at maximum exposure temperatures of 440°F, 465°F, and 490°F. A ply-by-ply inspection was conducted to evaluate the progression of damage through the thickness direction of the panel. The damage was considered removed when the predicted strength was above a go/no-go level for all locations within a ply. Once this condition was met, a scarfed repair was performed on the panel. On the panel that was exposed at 490°F, the go/no-go condition was not reached for every location, but inspection had to be stopped because of repair size limitations on the panel. Tensile testing showed that there was no statistically significant difference between the strength of the repaired panels and an undamaged control panel with a 95% confidence interval. A statistically significant difference was found between the repaired panels and a panel with localized thermal exposure (480°F). These results indicate that the damage was removed by the FTIR inspection and subsequent repair, validating that FTIR is a useful tool for guiding repair of ITD in CFRP.

Fluorescence measurements and contact angle measurements were also investigated as possible ITD detection methods, but neither technique was sensitive enough to be useful for detecting ITD.

17. Key Words	18. Distribution Statement
Composites, Damage, Inspection, Fourier transform infrared spectroscopy, Nondestructive inspection, Incipient thermal damage	This document is available to the U.S. public through the National Technical Information Service (NTIS), Springfield, Virginia 22161. This document is also available from the Federal Aviation Administration William J. Hughes Technical Center at actlibrary.tc.faa.gov.

19. Security Classif. (of this report)	20. Security Classif. (of this page)	21. No. of Pages	22. Price
Unclassified	Unclassified	66	

Form DOT F 1700.7 (8-72) Reproduction of completed page authorized

ACKNOWLEDGEMENTS

The authors would like to acknowledge and thank the following people for their help with this project: Paul Shelley and Paul Vahey from The Boeing Company analytical chemistry group for their help with Fourier transform infrared (FTIR) analysis and model development; Mark Bradley, John Spalding, and Mary Vargas from the Boeing repair group for providing use of their facilities for this research; Alan Rein and John Seelenbinder from Agilent Technologies for their help with questions relating to the ExoScan™ and help with FTIR analysis.

TABLE OF CONTENTS

			Page
EXECUTIVE SUMMARY			vi
1.	INTRODUCTION		1
	1.1	Background	1
	1.2	Project History	1
	1.3	Project Objective	1
2.	EXPERIMENTAL PROCEDURE		2
	2.1	Sample Preparation	2
		2.1.1 SBS Sample Preparation	2
		2.1.2 Panels With Localized Thermal Damage	3
		2.1.3 Sample Sanding	4
	2.2	Inspection Methods	4
		2.2.1 Fluorescence Measurements	4
		2.2.2 CA Measurements	5
		2.2.3 FTIR Measurements	6
		2.2.4 FTIR Guided Panel Inspection for ITD	8
	2.3	Repair of Inspected Panels	9
	2.4	Mechanical Testing of Panels	10
		2.4.1 Tensile Testing Sample Preparation	11
		2.4.2 Tensile Testing Procedure	12
3.	RESULTS		12
	3.1	Fluorescence Measurements	12
	3.2	CA Measurements	14
	3.3	FTIR MEasurements	15
		3.3.1 FTIR Measurements on Resin-Rich and Fiber-Rich Surfaces	15
		3.3.2 Sanding Variable Study	17
		3.3.3 Model Development	22
		3.3.4 Model Refinement	26
	3.4	Panel Mapping Results	31
		3.4.1 Surface Mapping of Panels	31

3.4.2 Low-Exposure Panel Mapping 32
3.4.3 Medium-Exposure Panel Mapping 34
3.4.4 High-Exposure Panel Mapping 35

3.5 Tensile Testing of Panels 36

4. SUMMARY OF RESULTS 38

4.1 Fluorescence Measurements 38
4.2 CA Measurements 39
4.3 FTIR 39

5. REFERENCES 41

APPENDICES

A—TENSILE TEST RESULTS

LIST OF FIGURES

Figure		Page
1	Setup for localized heating of the composite panels	3
2	A fluorescence measurement and a fluorescence measurement setup	5
3	Schematic showing camera view with respect to fiber direction	5
4	The VCA Optima Goniometer and side-view of a drop as viewed from the goniometer camera, showing CA measurements in the upper-left corner of the image	6
5	Effect of sample orientation on FTIR measurements collected on resin-poor surfaces	7
6	A grid system for mapping and an FTIR mapping measurement	8
7	Repaired panels	10
8	Ultrasound image of repaired panels	10
9	The 45° tensile test coupons for repaired control panel	12
10	Fluorescence spectra of SBS exposed at 445ºF and 475ºF for various times	13
11	SBS retention versus λ_{MAX}	13
12	Average CA measurements on SBS samples with thermal treatment temperatures of 415°F, 445°F, 475°F, and 505°F for various times, fluids, and surfaces	15
13	FTIR spectra on resin-rich surface of composite with various levels of thermal exposure	16
14	Raw FTIR spectra on sanded samples showing representative spectra of low, medium, and high damage samples	17
15	SBS samples with a well-sanded surface and a poorly sanded surface	18
16	Examples of spectral artifacts that influenced F_{SBS} predictions	19
17	Stereo micrographs of sanded surfaces using orbital sander parallel to fibers and perpendicular to fibers	20
18	Scores plot for the sanding variables grit size, sanding method, and direction relative to fiber	21
19	FTIR preprocessed with Savitzky-Golay first derivative and seven smoothing points	22
20	Predicted vs. actual F_{SBS} of a calibration set using a PLS regression with five PCs and a frequency range of 1700–950 cm^{-1}	24
21	Predicted vs. actual F_{SBS} for the evaluation set	25
22	Histogram of relative error in prediction of evaluation set F_{SBS} from calibration model	26
23	Model 1 prediction on medium-exposure panels	27
24	Comparison of model predictions for medium-exposure panel for surface ply, 1st ply down, and 2nd ply down	30

25 Surface maps made on a resin-rich tooled surface and a fiber-rich sanded surface predicted with model 4 32

26 Ply-by-ply map of predicted damage on a low-exposure panel; the surface map was predicted using model 4 and subsurface plies were predicted using model 5 33

27 Ply-by-ply map of predicted damage on medium-exposure panel: the surface map was predicted using model 4 and sub-surface plies were predicted using model 5 34

28 Ply-by-ply map of predicted damage on a high-exposure panel: the surface map was predicted using model 4, and subsurface plies were predicted using model 5 35

29 The 45° tensile test results 37

30 Failed tensile samples of a thermally damaged panel and a repaired high-exposure panel 38

LIST OF TABLES

Table		Page
1	SBS thermal exposure	2
2	Polar and dispersive surface energies for CA fluids	6
3	F_{SBS} data for calibration and evaluation for BMS 8-276 SBS sets	23
4	PLS models and parameters	28
5	Model predictions of SBS evaluation set	28

LIST OF ACRONYMS

CA	Contact angle
CAI	Compression after impact
CFRP	Carbon fiber-reinforced plastic
DI H_2O	Deionized water
DIM	Diiodomethane
DVD	Double vacuum debulking
F_{SBS}	Measured short-beam strength
FTIR	Fourier transform infrared (spectroscopy)
IR	Infrared
ITD	Incipient thermal damage
LIF	Laser-induced fluorescence
M-Distance	Mahalanobis distance
MVA	Multivariate analysis
NDE	Nondestructive evaluation
PC	Principal component
PCA	Principal component analysis
PLS	Partial least squares
RMS	Root mean square
RMSECV	Root mean square error of cross-validation
SBS	Short-beam strength
SECV	Standard error of cross-validation
UW	University of Washington

EXECUTIVE SUMMARY

Current nondestructive evaluation methods for composites, such as ultrasound, have difficulty detecting the onset of incipient thermal damage (ITD). Phase I of this project was a collaboration between The Boeing Company and A2 Technologies to investigate the use of a handheld Fourier transform infrared (FTIR) spectrometer for detecting and repairing ITD in composites. The FTIR works by measuring chemical changes to the polymer matrix as a function of the time and temperature of exposure. In Phase I, a successful correlation between FTIR spectra and short-beam strength (SBS) was established and used to generate models to predict the level of damage based on the FTIR measurements.

Phase II of the project was conducted at the University of Washington (UW) in collaboration with Boeing. Phase II involved using the FTIR measurements to guide the repair of panels that had been subjected to various levels of localized thermal damage. The model in Phase I was developed for a resin-rich surface of a BMS 8-276 composite material; however, during repair, a fiber-rich surface that gave significantly different FTIR measurements was exposed. To conduct Phase II, a new model was generated by UW to correlate SBS to FTIR measurements on sanded surfaces. A good correlation was found, and a model to predict damage on the fiber-rich surface was created. Using the model, a ply-by-ply inspection of the thermally damaged panels was performed. The inspection was continued until none of the measurements in a ply were below a go/no-go value. The one exception was in the case of the high thermal exposure in which the depth of the damage exceeded the repair size limit and inspection was stopped while the panel could still be repaired.

To determine if the damage was removed by the inspection process, tensile testing was performed on the repaired samples with controls used as references for an undamaged panel and a repaired panel. Initially, the plan was to test the repaired panel and a duplicate damage panel for each exposure level to judge how well damage had been removed. However, while preparing test samples, it was found that repaired and damaged panels had different laminate stacking sequences, making it impossible to compare. Tensile testing of repaired samples and comparison to control panels appeared to show that the damage had been removed from the panels that were inspected and repaired. However, more testing is recommended to confirm this result because of the limited sample size.

In conclusion, FTIR is a feasible method to inspect for ITD and to guide repair of composites with ITD.

1. INTRODUCTION

1.1 BACKGROUND

Previous research shows that a range of thermal exposure of composites can cause mechanical property loss that is undetectable by traditional nondestructive evaluation (NDE) methods, such as ultrasound [1, 2]. This early stage of thermal damage is known as incipient thermal damage (ITD). The ITD of composites can reduce mechanical properties, such as flexural strength, compression after impact (CAI), and interlaminar shear strength [3–7]. Characterization techniques, such as Fourier transform infrared (FTIR) spectroscopy, laser-induced fluorescence (LIF) of the epoxy matrix, fluorescent thermal damage probes, Raman spectroscopy, nuclear magnetic resonance, and thermoelastic characterization, have all been used to detect and evaluate the ITD of composites [2–5, 7–10]. The two techniques that have been investigated as having the most potential for field inspections are FTIR and LIF [1–3].

The work presented in this report focused on investigating the use of a handheld FTIR as a guide for repairing a panel with ITD.

1.2 PROJECT HISTORY

Phase I began as a collaboration between A2 Technologies (now part of Agilent Technologies), the Federal Aviation Administration, Sandia Airworthiness Center, the University of Delaware, and The Boeing Company to investigate the use of the handheld ExoScan™ FTIR unit (Agilent model 4100) for the inspection of ITD and other matrix-related degradation (e.g., ultraviolet light). During Phase I of the project, composite panels were fabricated, thermally exposed, and mechanically tested. The preliminary work to correlate the mechanical properties of the thermally exposed samples to the FTIR spectra was also performed. Short-beam strength (SBS) was chosen as the mechanical property to correlate to the FTIR spectra based on previous research [2, 11]. The SBS measurements were performed at the University of Delaware Center for Composite Materials. After A2 Technologies became a part of Agilent, Phase II was passed on to the University of Washington (UW) with assistance from Boeing. In Phase II, a model for use on the fiber-rich sanded surface was developed. Panels with localized ITD were inspected using the FTIR to determine the location of the damage for removal; after all damage was removed, the panels were repaired. Mechanical testing was then performed to determine if the inspection process had successfully removed the damage.

1.3 PROJECT OBJECTIVE

The primary goal of the project was to investigate the use of FTIR to guide the removal of ITD from a composite panel. This was accomplished by developing a model to relate FTIR measurements to SBS and then inspecting panels with localized thermal exposures using the model to estimate the damage level. In addition, fluorescence and contact angle (CA) measurements were also investigated as possible alternatives or supplements to the FTIR inspection for ITD.

2. EXPERIMENTAL PROCEDURE

2.1 SAMPLE PREPARATION

2.1.1 SBS Sample Preparation

Unidirectional 24-ply composite panels were fabricated using BMS 8-276 prepreg and cured at 350°F by Boeing. The panels were inspected using a through transmittance, tone-burst waterjet, transit-time ultrasound scan system with 140 dB dynamic range and 5 MHz scans to ensure the integrity of the panel. Panels were then cut into 2.85 cm x 0.95 cm x 0.48 cm SBS samples.

The samples were subjected to a prescribed thermal exposure in a Lindberg/Blue M MO1450A convection oven. The exposure time and temperature for each set is shown in table 1. The exposure times and temperatures were chosen using a design of experiments to ensure that the range of exposures was statistically relevant and representative of potential real world exposures. Six SBS samples were exposed for each sample set. Three of the samples from each set were subjected to SBS testing, and three were used for FTIR measurements. The thermal exposures were performed during Phase I of the project by the University of Delaware [11].

Table 1. SBS thermal exposure [11]

Calibration Set			
Sample	Temp. (°F)	Time (min)	Coupon label
1	385	30	C1-1 to -6
2	445	30.00	C2-1 to -6
3	505	30.00	C3-1 to -6
4	415	48.11	C4-1 to -6
5	475	48.11	C5-1 to -6
6	535	48.11	C6-1 to -6
7	385	77.14	C7-1 to -6
8	445	77.14	C8-1 to -6
9	505	77.14	C9-1 to -6
10	355	123.7	C10-1 to -6
11	415	123.7	C11-1 to -6
12	475	123.69	C12-1 to -6
13	385	198.3	C13-1 to -6
14	445	198.34	C14-1 to -6
15	355	318.05	C15-1 to -6
16	415	318.05	C16-1 to -6
17	475	318.05	C17-1 to -6
18	325	510.00	C18-1 to -6
19	385	510	C19-1 to -6
20	445	510.00	C20-1 to -6

Evaluation Set			
Sample #	Temp. (°F)	Time (min)	Coupon label
1	415	30	E1-1 to -6
2	475	30.00	E2-1 to -6
3	535	30.00	E3-1 to -6
4	385	48.11	E4-1 to -6
5	445	48.11	E5-1 to -6
6	505	48.11	E6-1 to -6
7	355	77.14	E7-1 to -6
8	415	77.14	E8-1 to -6
9	475	77.14	E9-1 to -6
10	385	123.7	E10-1 to -6
11	445	123.69	E11-1 to -6
12	355	198.3	E12-1 to -6
13	415	198.3	E13-1 to -6
14	475	198.34	E14-1 to -6
15	325	318.05	E15-1 to -6
16	385	318.05	E16-1 to -6
17	445	318.05	E17-1 to -6
18	355	510	E18-1 to -6
19	415	510	E19-1 to -6
20	475	510.00	E20-1 to -6

2.1.2 Panels with Localized Thermal Damage

Six 24-ply panels were fabricated using BMS 8-276 graphite-epoxy prepreg cured at 350°F for 150 minutes at Boeing. To create ITD in a localized hotspot, individual panels were covered with a heat blanket and layers of insulation were stacked on top of the blanket in the center of the panel. The setup was then placed inside a vacuum bag and heating was performed under vacuum. Ten thermocouples were placed on the panels to measure the temperature at various locations. The panels were heated for 1 hour each at a maximum exposure temperature of 440°F, 465°F, or 490°F. Because the exposure time was the same, all panels will herein be referred to as low, medium, and high exposure based on their maximum exposure temperatures with low and high referring to the 440°F and the 490°F panels, respectively. The panels were damaged by Boeing during Phase I of the project [11]. The heating setup and progressive stages are shown in figure 1.

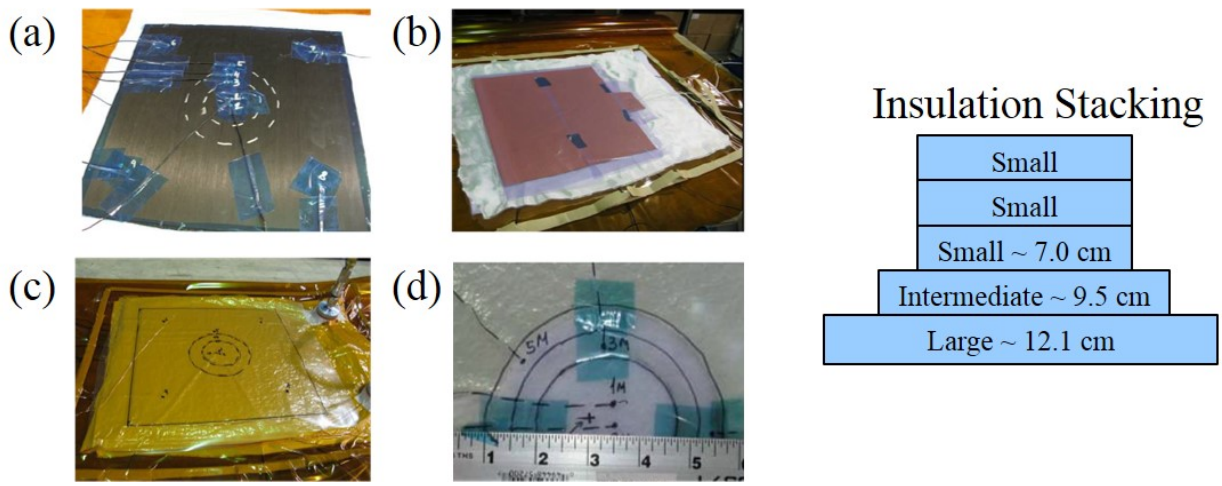

Figure 1. Setup for localized heating of the composite panels: (a) thermocouple placement, (b) heat blanket placement, (c) vacuum bagged panel, and (d) insulation stacking [11]

Panels were inspected using ultrasound prior to and after thermal exposure. No delaminations were found in any of the panels, even after thermal exposure.

Two panels were subjected to the same exposure level for each exposure with the intention that one would be inspected with FTIR and repaired, and the other would be left damaged for mechanical testing. When the panels were given to UW, it was thought that the layup was identical for all the panels; however, after the samples were cut up for mechanical testing, it was discovered that there were two different sets of layups. The panels labeled NDE 1–3 by Boeing had a quasi-isotropic layup, and the panels labeled NDE 4–6 had all the plies oriented in the 0° direction. The unidirectional panels were the ones inspected by FTIR; therefore, mechanical testing was focused on the unidirectional panels.

2.1.3 Sample Sanding

2.1.3.1 Sanding Variable Study

The surface finish of the part can influence the FTIR measurements, and a good match of surface finish between calibration and inspected parts is needed to obtain good measurements [1, 2, and 11]. Several sanding variables were investigated to evaluate the sensitivity of the ExoScan FTIR to the surface conditions. The variables included grit size, sanding method (hand versus orbital sanding), and direction of sanding relative to fiber orientation. In each case, only the variable of interest was changed within the set. For the grit size evaluation, 180-, 240-, and 320-grit sandpapers were used. For the sanding method and sanding direction studies, the 180-grit sandpaper was used. The sanding variables experiments were carried out on samples that had not been subjected to thermal exposure.

2.1.3.2 Sanding of SBS Calibration Samples and Panels

SBS calibration samples were sanded using an orbital sander with 180 grit sandpaper to closely match repair surface finishes. To match the surface finish with the SBS samples, the panels with localized damage were sanded using the same process.

2.2 INSPECTION METHODS

2.2.1 Fluorescence Measurements

Fluorescence measurements were made using a StellarNet BLUE-Wave UVN spectrometer with a R600-8-UVVIS SR reflectance probe. The probe contains a 600 μm read fiber (detector) at the core and is surrounded by seven fibers that focus the excitation source onto the sample. A 470 nm LED was used as the excitation source for the fluorescence measurements. A 470 nm bandpass filter with a 50 nm bandwidth (Edmund Optics) was used to remove reflections of the excitation source that could interfere with the detection of the fluorescence spectrum. The probe was rested on the surface of the sample at a 45° angle, as shown in figure 2. The spot size of the excitation light was approximately 3 mm. The integration time for the detector was set to 5000 ms, and nine scans of each spectrum were averaged. The samples were constrained so that they could only translate in one dimension. Fluorescence measurements were taken on toolside (resin-rich) and sanded (fiber-rich) surfaces. Three measurements were taken per sample.

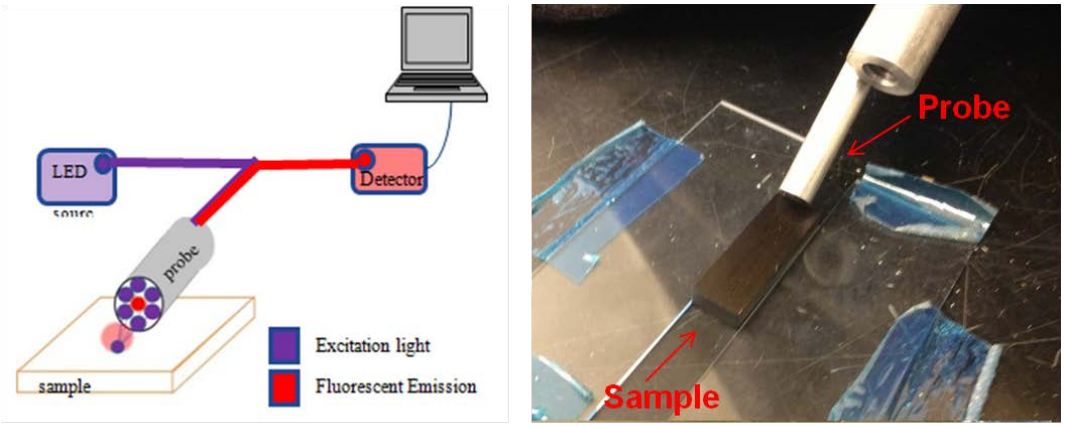

(a) (b)

Figure 2. A (a) fluorescence measurement and a (b) fluorescence measurement setup

2.2.2 CA Measurements

For traditional side-view CA analysis, SBS specimens were acetone wiped within 1 hour of drop application. The stage was always confirmed to be level. Drops of 1 µL volume were dispensed from the syringe and placed onto the test surface by raising the stage and catching the drops. The drop orientation, with respect to the goniometer camera, was perpendicular to the fiber direction, as shown in figure 3. The drops were applied to both a resin-rich toolside and a fiber-rich sanded surface.

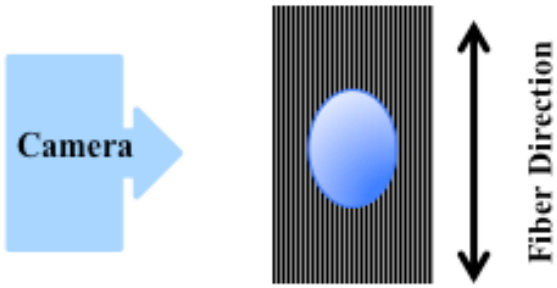

Figure 3. Schematic showing camera view with respect to fiber direction

The fluids used for CA measurement were deionized water (DI H_2O) and diiodomethane (DIM). These fluids were chosen because of their diversity in polar and dispersive components of surface energy. DI H_2O is mostly polar and DIM is mostly dispersive, as shown in table 2. An image of the side view of the drop was frozen at a predetermined time of 5 seconds, and the CAs were measured using the goniometer software. Figure 4 shows the instrument and an example drop image with measured CAs. A total of 10 measurements (5 drops) were averaged for each CA value reported. CAs were measured on toolside and sanded surfaces.

Table 2. Polar and dispersive surface energies for CA fluids

Fluid	γ^p (mJ/m^2)	γ^d (mJ/m^2)	γ^{tot} (mJ/m^2)
Deionized Water [12]	50.2	22.0	72.2
Diiodomethane [13]	0	50.8	50.8

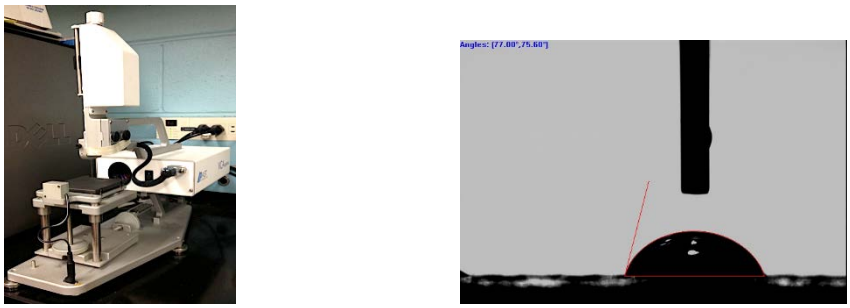

(a) (b)

Figure 4. The (a) VCA Optima Goniometer and (b) side-view of a drop as viewed from the goniometer camera, showing CA measurements in the upper-left corner of the image

2.2.3 FTIR Measurements

To use the FTIR for thermal damage inspection of carbon fiber-reinforced plastic (CFRP) parts, a calibration model correlating the FTIR spectra to a property of the composite or level of thermal exposure was needed. For this study, SBS measurements were chosen as the property to correlate with the FTIR spectra to assess thermal damage because SBS had been shown to correlate to thermal damage using the FTIR Phase I of the project and by other sources [2, 11].

2.2.3.1 SBS Measurements

SBS measurements on the calibration and evaluation sets described in section 2.1.1 were performed at the University of Delaware in the first year of the project. SBS measurements were performed according to ASTM D2344. The measurements were taken on an Instron 4484 load frame using an SBS testing fixture with a 1.84 cm span and a displacement rate of 0.13 cm/min [11]. The measured short-beam strength (F_{SBS}) was determined from equation 1 [14]:

$$F_{SBS} = 0.75 \times \frac{P_m}{b \times h} \tag{1}$$

where P_m is the maximum load, and b and h are the width and height of the sample, respectively.

2.2.3.2 FTIR Measurements on SBS Calibration Set

The FTIR measurements in this report were performed by UW using a handheld Agilent Technologies ExoScan 4100 handheld FTIR. SBS specimens were acetone wiped and dried with a Dupont™ Sontara® aerospace-grade wipe prior to measurement to remove possible

contamination (e.g., sanding debris, dust, dirt, and oil). The ExoScan was configured for diffuse reflectance, which has been shown to obtain the best results on sanded composite surfaces [11]. The baseline of the measurements varied greatly depending on how the FTIR was oriented relative to the fiber direction. The samples were oriented to minimize the baseline variations; this helped reduce the variability between measurements [11]. The effect of fiber orientation on the FTIR spectra is shown in figure 5.

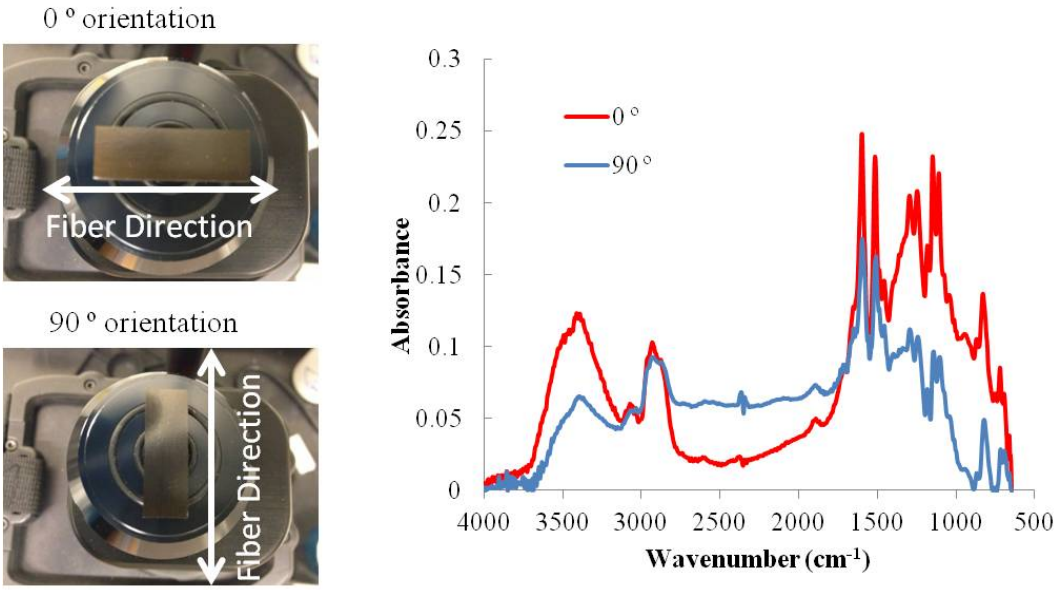

Figure 5. Effect of sample orientation on FTIR measurements collected on resin-poor surfaces

Though the baseline was lower for the 0° orientation, the baseline variation between measurements was found to be minimized when the handle of the FTIR was perpendicular to the fiber direction. The Phase I report states that a similar orientation was used on the sanded samples [11]. The spectra were collected from the mid-infrared region (4000–650 cm^{-1}) using 90 scans with 16 cm^{-1} resolution. Three measurements were taken on each of the three samples within a given thermal exposure set for a total of nine measurements per set.

2.2.3.3 Sanding Variable Study

The FTIR spectra for the sanding variable samples discussed in section 2.1.3.1 were imported into the GRAMS IQ™ multivariate analysis (MVA) program (Thermo Fischer Scientific™). The spectra were pre-processed using mean-centering, multiplicative scatter correction, and a Savitzky-Golay first derivative with a seven-point smoothing algorithm. The spectra were analyzed in the 1700-950 cm^{-1} wavelength region. Principal component analysis (PCA) was used to analyze the variance between the spectra to determine how sensitive the measurements were to the sanding variables.

2.2.3.4 Thermal Exposure Calibration Model and Model Validation

FTIR spectra measurements on the SBS calibration set were imported into the GRAMS IQ software. The spectra were then pre-processed using mean-centering, multiplicative scatter correction, and a Savitzky-Golay first derivative with a seven-point smoothing algorithm. The calibration model was generated by performing a partial least squares (PLS) regression to correlate FTIR spectra to F_{SBS}. Several model parameters were varied to understand their impact on the predictive capabilities of the model. Those parameters included the range of F_{SBS} values contained in the calibration set, the number of principal components (PCs) used in the model, and the frequency range, expressed in wavenumbers (cm^{-1}), analyzed. These parameters were varied, as discussed in section 3.3.3, to determine a good model for inspection of the panels. The regression model was validated by using the model to predict the F_{SBS} values of the independent evaluation SBS set from spectra measured on the independent set.

2.2.4 FTIR Guided Panel Inspection for ITD

2.2.4.1 Surface Mapping of Damaged Panels

Tape was placed around the edges of the panels with tick marks spaced every 1.27 cm (0.5″). The marks created a grid for the mapping. FTIR measurements were taken at every point in the grid. Rulers were used to align the head of the FTIR with the appropriate point on the grid. The SBS values from the FTIR measurements were predicted using the calibration model developed from the SBS samples using GRAMS IQ Predict software. Images of the grid system and FTIR measurement during the mapping are shown in figure 6. Because of the large area for the initial surface mapping, only one FTIR spectrum was measured per grid point.

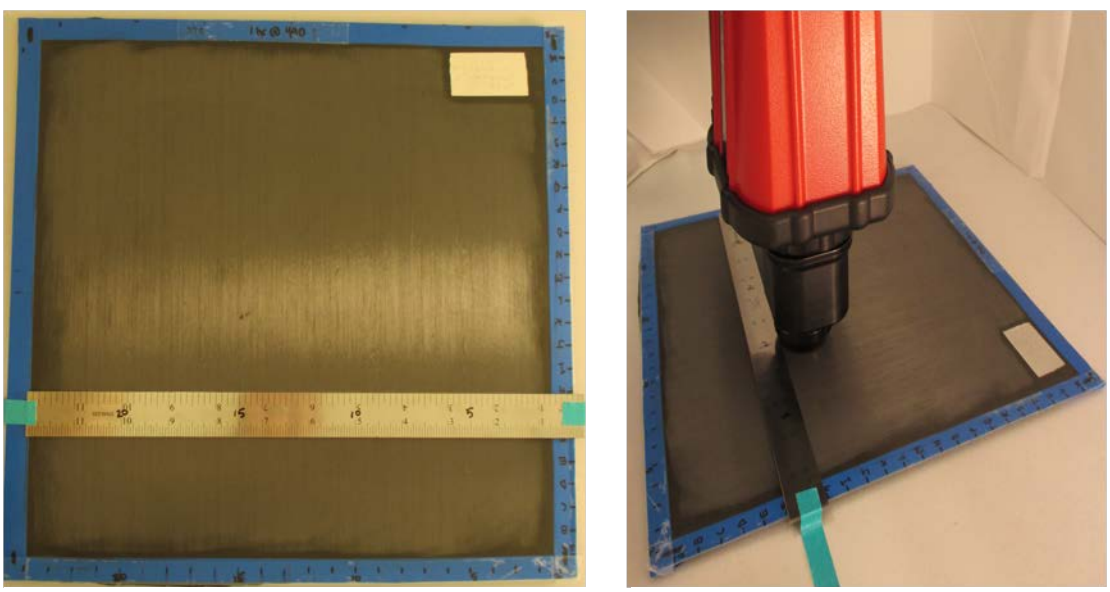

(a) (b)

Figure 6. A (a) grid system for mapping and (b) an FTIR mapping measurement

2.2.4.2 Ply-by-Ply Inspection of Panels With ITD

The area on a panel to be inspected was determined from the surface mapping. The damaged area was defined by establishing a go/no-go threshold. The defining of the go/no-go threshold is discussed in section 3.4.2. The damage was considered removed if the measurement was above the threshold, and that area was not included in the inspection. Once the initial damage area was identified, that area was sanded down to the first ply below the surface. After cleaning the surface with an acetone wipe and letting it dry, the FTIR inspection of the ply was performed using the same grid system as the surface mapping. However, in the ply-by-ply inspection, three measurements were taken at every grid point instead of the one used for the surface map. After completing all the measurements for a ply, the results were reviewed and a new damaged area to inspect was identified using the go/no-go threshold. That area was sanded to the next ply down and the process was repeated until all measurement in the area passed go/no-go threshold or the maximum repair size for the scarfed repair was reached.

2.3 REPAIR OF INSPECTED PANELS

After the inspection on a panel was completed, the area that had been sanded to remove damage was again sanded to produce a 30:1 scarf angle for the repair patch. Each ply was traced onto a transparent template; a master template with all the plies was also traced out. Patch plies were cut using the templates from BMS 8-276 prepreg. The repair patch was created by stacking the individual plies together according to the master template. The high-exposure patch was greater than 6 plies and was subjected to a double vacuum debulking (DVD) process to remove volatiles from the patch that could become trapped during the curing process because of the thickness of the patch. The low- and medium-exposure panels had repair sizes of 2 and 4 plies, respectively, and did not need to undergo the DVD process. Prior to the repair, the scarfed panels were dried in an oven at 300°F for 240 minutes to remove moisture that could affect bond quality. The repair was performed by laying a MetlBond® 1515-3M adhesive in the scarfed-out area of the panel. The adhesive was cut so that it extended approximately 1.3 cm beyond the diameter of the top ply on the repair patch. A fiberglass scrim was placed on top of the adhesive to help facilitate the removal of volatiles during the repair. The CFRP patch was then placed in the repair area, taking care so that the orientation of the fibers was correct. The panel was placed on a caul plate; release film, heat blanket, and insulation were placed on top of the panel. The setup was similar to the thermal exposure to damage the panels described in section 2.1.2, except the extra insulation layers were not stacked on top of the heat blanket. To monitor the temperature, 4 thermocouples were placed just outside the repair area. The repair cure was then performed using a HEATCON® hot bonder. The cure was carried out under vacuum at 350°F for 150 minutes. The repaired panels are shown in figure 7.

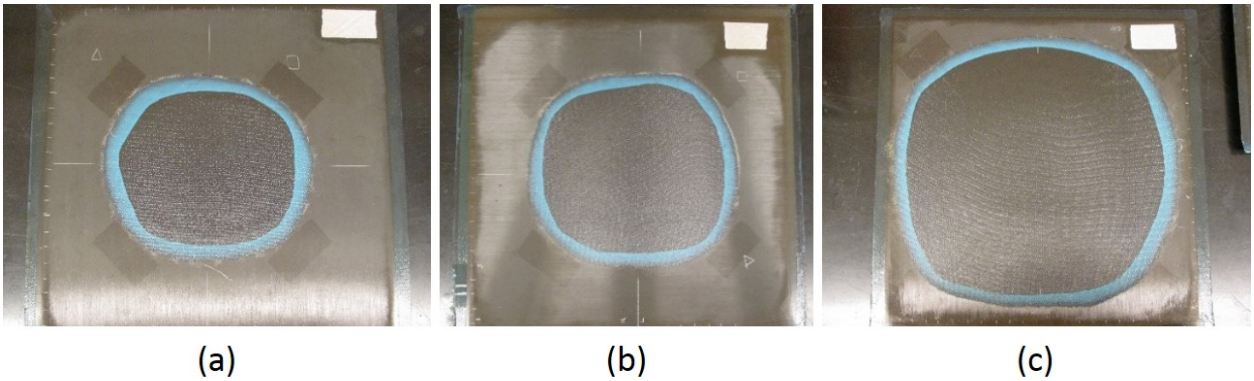

Figure 7. Repaired panels: (a) low exposure (2 plies), (b) medium exposure (4 plies), and (c) high exposure (14 plies)

After the repair, the panels were inspected using ultrasound. Ultrasound cannot be used to determine that a good bond was made, but it can be used to look for delamination or porosity that could affect the performance of the repair. The ultrasound inspection was performed at Boeing using a 2.5″ focused through transmission ultrasound at 5 MHz using a 6″ water path and 0.04 resolution. The ultrasound results are shown in figure 8.

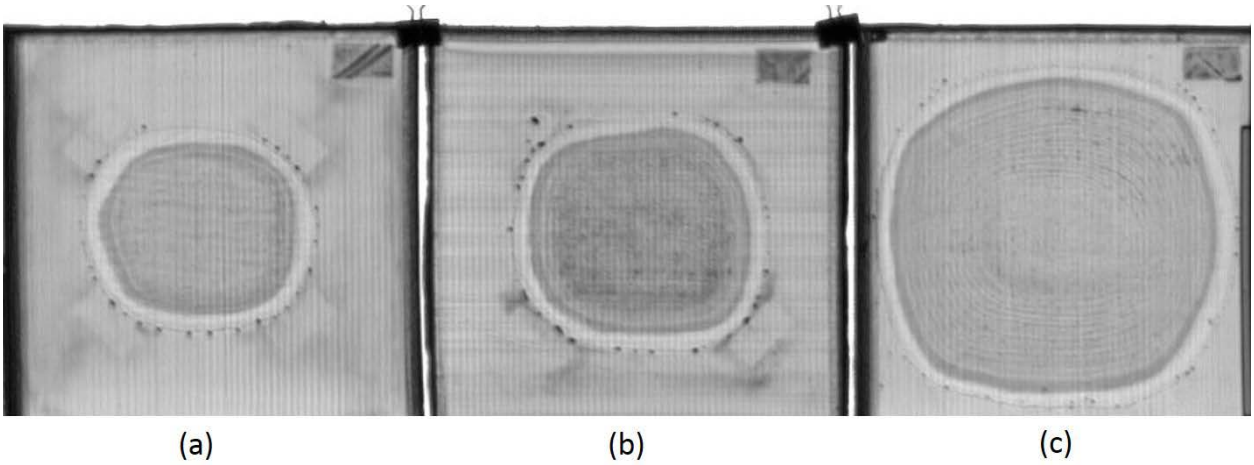

Figure 8. Ultrasound image of repaired panels: (a) low-exposure panel, (b) medium-exposure panel, and (c) high-exposure panel

Figure 8 shows that the repaired panels had no significant defects observable by ultrasound, although there is some porosity around the edges, especially for the low- and medium-exposure panels.

2.4 MECHANICAL TESTING OF PANELS

Though the FTIR measurements were correlated to SBS measurements on uniformly heated SBS samples, it was determined that SBS testing may not be the best test method to measure the strength of the panels. The reason for this was that the maximum damage was on or close to the surface of the panels, whereas for SBS, the maximum shear stress occurs near the center of the

panel and minimal stress at the surface. Several different testing methods were considered, including flexural, un-notched edge compression, CAI, and tensile testing. The two compression tests were ruled out because the sample size was so large that only one measurement could be obtained per panel. Given that the panels being tested were unidirectional, or at least thought to be before they were cut up (see section 2.1.2), it was thought that tensile with fibers oriented at 45° would provide a good measure of matrix properties that would be affected by ITD. Tensile testing also allowed for testing of more samples than a compression test would have.

2.4.1 Tensile Testing Sample Preparation

2.4.1.1 Additional Panels Fabrication and Preparation

In addition to the six panels provided by Boeing, it was determined that three more panels were necessary to have comprehensive test results. The additional panels consisted of a panel with no thermal exposure, a repaired panel with no thermal exposure, and another panel with localized thermal damage. The panel with no thermal exposure was needed to give a baseline strength for a panel with no damage. The repaired panel with no thermal exposure was to give a measure of how the repair alone affected the strength of the panel. The additional panel with localized thermal damage was originally fabricated to verify that the tensile test was sensitive to the damage before testing the panels that were inspected and repaired. This panel was also used to represent a damaged panel in the testing after the duplicate damage panels from Phase I were found to be incompatible with the panels that were inspected and repaired because of significant differences in the stacking sequence (see section 2.1.2).

All panels were fabricated at UW using BMS 8-276, laid up as unidirectional panels, and contained 24 plies like the panels from Phase I. The panels were cured in an autoclave in a vacuum bag using the following cure cycle:

- The pressure was increased to 85 psi when at room temperature.
- After pressure was reached, the temperature was increased to 350°F at a rate of 5°F/min.
- The temperature was held at 350°F for 150 minutes.

The repaired panel was milled so that plies would have a 30:1 scarf angle. The panel was milled 11 plies into the panel to create a large repair area. After milling, the panel was sanded using 180-grit merit sandpaper and an orbital sander to give a surface finish similar to the other repaired panels. The panel was then repaired using the same methodology as the high-exposure panel (see section 2.3).

The thermally damaged panel was created using the same procedure as described in section 2.1.2. The panel was exposed for 1 hour at 480°F, which was close to the high-exposure panel thermal exposure.

2.4.1.2 Tensile Test Sample Machining

All tensile samples were cut using a water-cooled diamond saw and oriented so that the fibers were angled at 45° to the lengthwise direction of the coupon. The tensile coupons were cut to be ~25 mm wide and had a length of approximately 200 mm. Six to seven tensile samples were

obtained from each panel. As much of the repaired area as possible was included in the coupon. Because of the circular nature of the repair area, some sections contained more of the repair area than others. The tensile coupons for the repaired control panel are shown in figure 9.

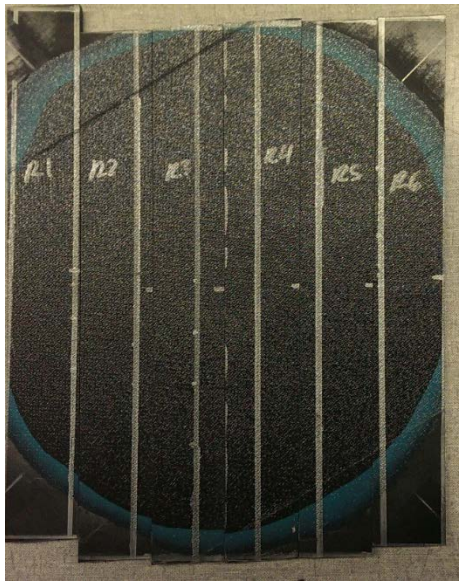

Figure 9. The 45° tensile test coupons for repaired control panel

2.4.2 Tensile Testing Procedure

Testing was performed in an Instron® 5500R test frame with a 100 kN load cell. Samples were first secured in the top wedge grip, and the load was zeroed. The sample was then clamped in the lower wedge grip. Rough emery cloth was placed at both ends of the sample to help improve gripping. Typically, after clamping both ends of the sample, a small load was detected in the load cell; as a result, the crosshead was displaced using the fine displacement control until only a small preload of approximately 100 N was applied. The preload was used to prevent a slip in the grip while the sample was first loading. The displacement was then zeroed. The tensile testing was conducted using displacement control with a crosshead displacement of 2 mm/min as specified in ASTM D3039 [15]. Data were collected using Blue Hill® software v.3.1.

3. RESULTS

3.1 FLUORESCENCE MEASUREMENTS

Figure 10 shows fluorescence spectra obtained from the resin-rich tooled surface of the SBS samples thermally exposed at 445ºF and 475ºF for various times. Note that no sample without thermal exposure was provided, so a reference as-cured sample was fabricated to provide a control. This sample is shown as the dashed line in the plots.

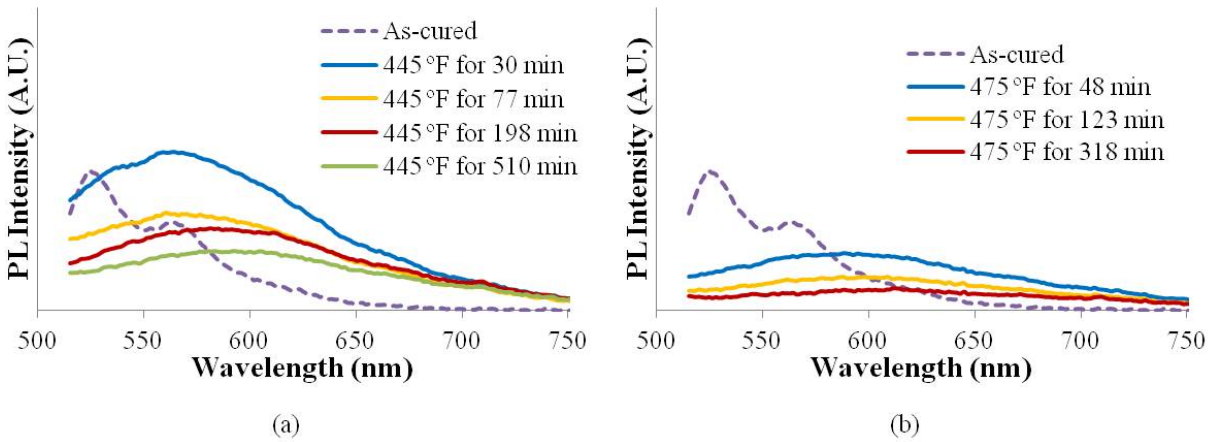

Figure 10. Fluorescence spectra of SBS exposed at (a) 445ºF and (b) 475ºF for various times

Two trends were observed in figure 10. The first trend was that the fluorescence intensity decreased as time and temperature of exposures increased. The exception to this was seen in the 415°F (not shown) and 445°F samples, in which the fluorescence intensity increased from that of the as-cured state during the initial thermal exposure. This behavior with which the intensity initially increases with thermal exposure and subsequently decreases was also observed by Fischer et al. [3]. However, in this case, it may also have been an artifact of using the independently fabricated sample. No matter what the reason, fluorescence intensity measurements were difficult to reproduce and were not reliable for quantifying damage. The second trend observed was that the wavelength at maximum intensity (λ_{MAX}) shifted to longer wavelengths (red shifts) with increasing exposure time and temperature. A plot of SBS retention versus λ_{MAX} is shown in figure 11.

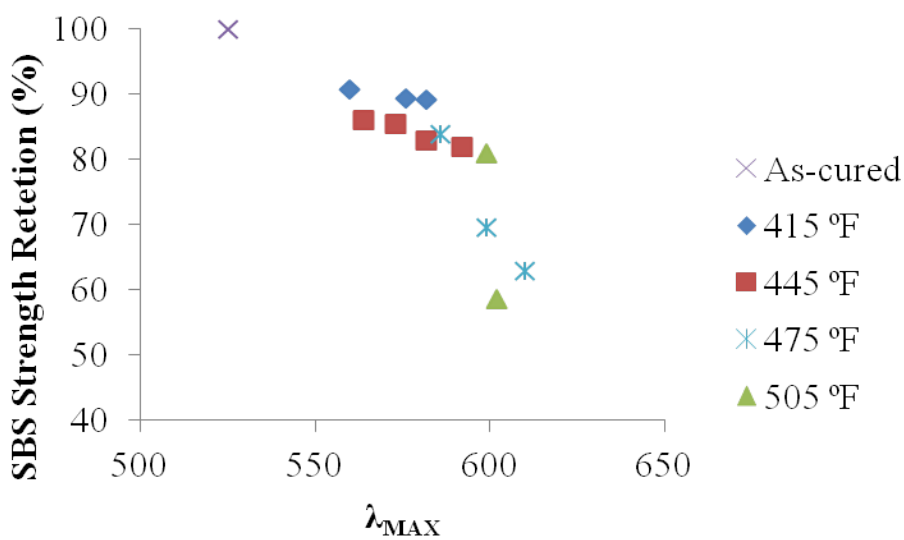

Figure 11. SBS retention versus λ_{MAX}

As shown in figure 11, as exposure time at a given temperature increased, a definitive red shift of λ_{MAX} occurred. However, this red shift did not monotonically correlate to SBS retention because

multiple SBS values were observed at a given λ_{MAX}. This means that the autofluorescence measurements may be useful for observing thermal exposure of the composite over a large area, but it would not allow for reliably estimating the amount of thermal damage as classified by SBS measurements. It is possible that a better correlation could be found using another matrix-dominated mechanical property measurement. Fischer et al. showed in their studies that a monotonic correlation was found between λ_{MAX} and flexural strength for their thermally damaged samples [3].

In addition, fluorescence measurements were made on the fiber-rich sanded surfaces of the SBS samples. No fluorescence was measurable on the fiber-rich surfaces. This may be a product of the lack of fluorescence signal available because of the lower volume fraction of resin or it may be that the source of the fluorescence was the oxidation products of the resin. Because of the many thermal degradation products of epoxy, the source of the autofluorescence is not well understood [3]. It is possible that fluorescence would be observable on the fiber-rich sanded surface using a different excitation wavelength or a more intense light source, but those options were not available at the time the measurements were made.

3.2 CA MEASUREMENTS

CA measurements were conducted on SBS specimens that were thermally treated at 415°F, 445°F, 475°F, and 505°F for various times. Increased time at these temperatures generally correlated with increasing thermal damage as measured by SBS values during research conducted during Phase I of this project. CAs were measured on the resin-rich toolside surface and the fiber-rich sanded surface. It was observed that CAs measured on sanded surfaces were lower than CAs measured on toolside surfaces. There was not, however, any significant correlation between SBS values and CA measurement. Figure 12 shows average DI H_2O and DIM CAs for the thermally treated SBS specimens at various temperatures and times.

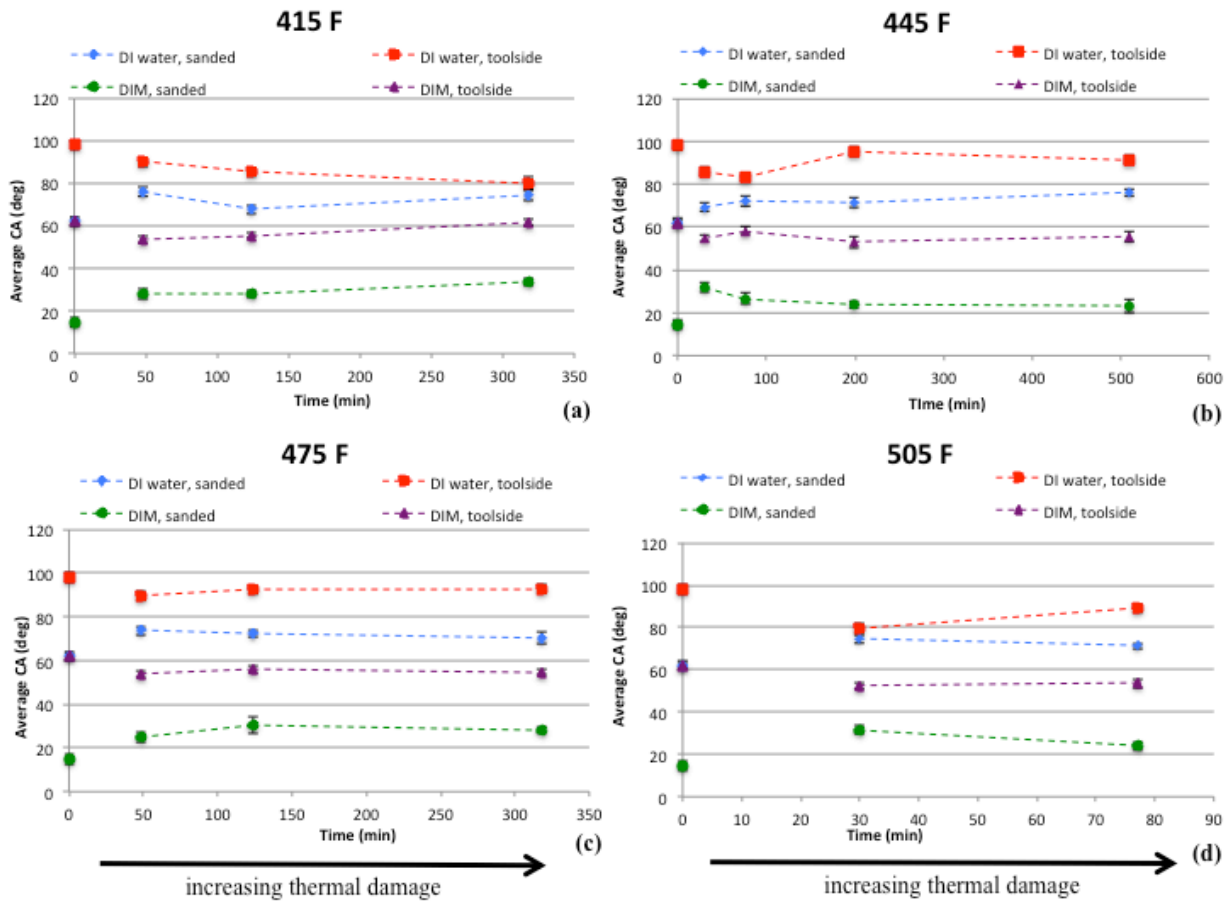

Figure 12. Average CA measurements on SBS samples with thermal treatment temperatures of (a) 415°F, (b) 445°F, (c) 475°F, and (d) 505°F for various times, fluids, and surfaces

3.3 FTIR MEASUREMENTS

3.3.1 FTIR Measurements on Resin-Rich and Fiber-Rich Surfaces

In Phase I of the project, FTIR measurements were made of the resin-rich tooled surface of SBS samples and panels with localized ITD. The resin-rich samples exhibited a visible change in the FTIR spectra around the carbonyl band 1720 cm^{-1} related to the oxidation of the epoxy due to thermal exposure [2, 11]. Figure 13 shows FTIR spectra for samples with varying levels of thermal damage.

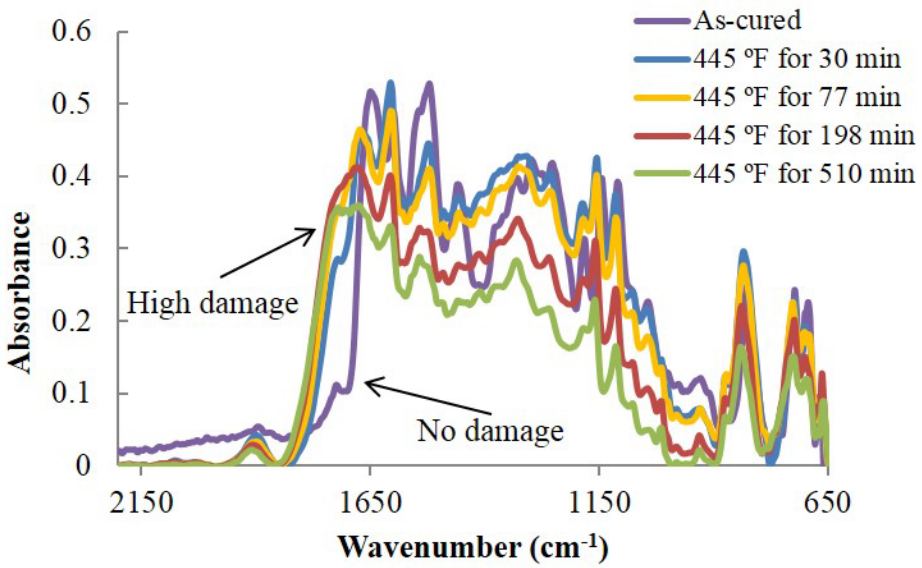

Figure 13. FTIR spectra on resin-rich surface of composite with various levels of thermal exposure

For an actual ply-by-ply inspection process, the measurements would be performed on fiber-rich sanded surfaces, for which the volume of resin is considerably less than on a tooled surface. Carbon fibers are also known to scatter infrared (IR) radiation [11]. In addition, oxidation of epoxy typically does not exceed 50–100 µm from the surface; therefore, the oxidation that is strongly observed in the resin-rich surface was removed with sanding of the surface [16]. As a result, the FTIR spectra obtained from measurements on sanded fiber-rich surfaces are significantly different from those obtained on resin-rich surfaces. Figure 14 shows FTIR spectra from samples representing different levels of thermal damage on sanded SBS samples similar to figure 13. C1 (blue) corresponds to a sample with little to no damage (F_{SBS} retention >95%), C3 (purple) corresponds to a moderate level of damage (F_{SBS} retention ~80%), and C9 (red) corresponds to a high level of damage (F_{SBS} retention <60%).

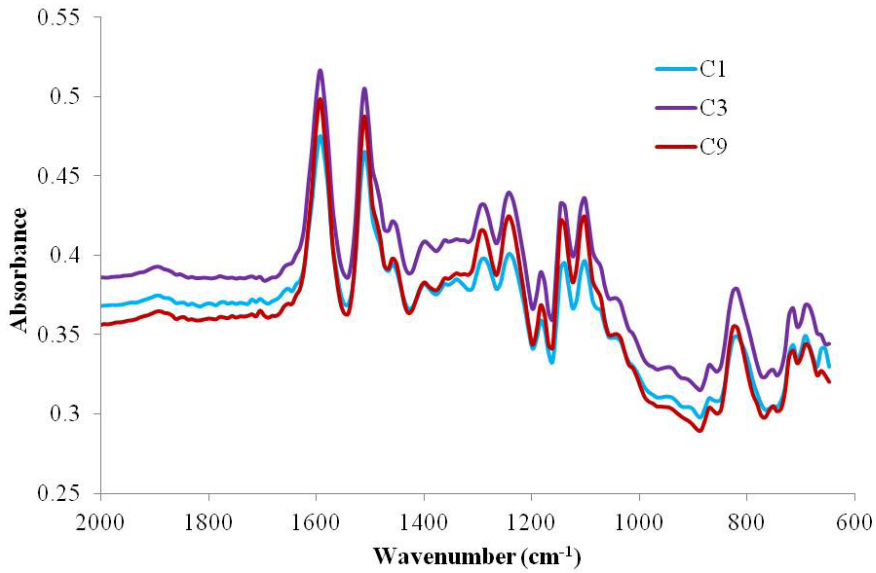

Figure 14. Raw FTIR spectra on sanded samples showing representative spectra of low (blue), medium (purple), and high (red) damage samples

Compared to the resin-rich surface in figure 13, in which it was easy to observe differences in the spectra with varying levels of damage, it is difficult to see clear differences between the spectra (besides small variations in the baseline) in figure 14, even though they exhibit significantly different F_{SBS}. This result is consistent with previous findings for sanded composite specimens [1, 2, 11]. As a result, the models developed for the resin-rich surface could not be applied for the fiber-rich surface, and it was necessary to create a new model that could be used for the fiber-rich surfaces of a ply-by-ply inspection.

3.3.2 Sanding Variable Study

It was discovered early on in the process that the variability of the sanding on the surface of the SBS samples made an impact on the FTIR measurements. Specifically, there was initial difficulty in sanding the SBS samples so that only one ply was exposed. In between plies, there is a thin layer that contains a higher resin-to-fiber ratio than in the plies. FTIR measurements taken in this resin-rich area were significantly different. A comparison of a well-sanded SBS sample and a sample with several plies exposed are shown in figure 15.

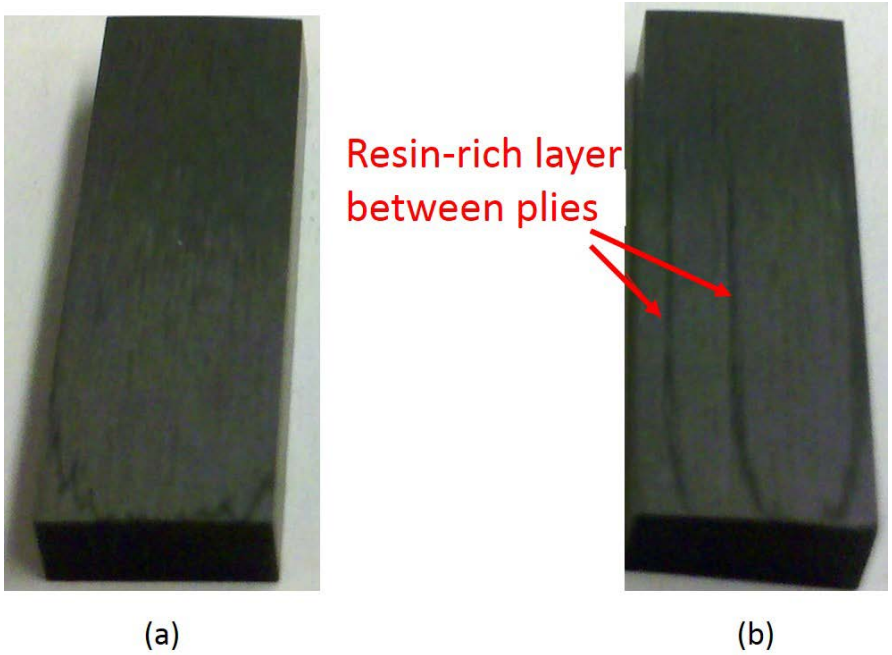

Figure 15. SBS samples with (a) a well-sanded surface and (b) a poorly sanded surface

Examples of spectral artifacts that affected model predictions are shown in figure 16. The blue curve represents spectra taken from a well-sanded sample. The green curve shows spectra in which the measured area was resin-rich compared to the well-sanded samples. The green oval indicates a large band around 1600–1700 cm^{-1} that only appears in samples with resin-rich areas. The other spectral artifact found to affect the measurements was noise. The red curve represents noisy spectra. The noisy spectra are difficult to distinguish from good spectra, but it can be observed with a close examination of the baseline (red oval). Noisy spectra can typically be mitigated by retaking a baseline reference spectrum. The spectra were offset vertically in the plot to make it easier to see the individual spectrum. How these artifacts affected predictions from the FTIR spectra is discussed in section 3.3.4.

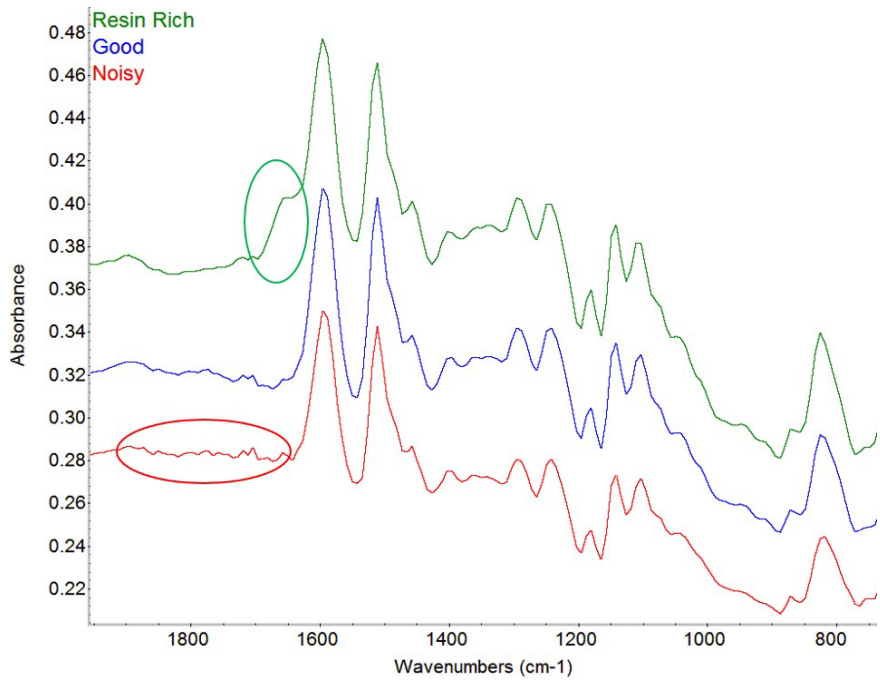

Figure 16. Examples of spectral artifacts that influenced F_{SBS} predictions

Because other studies had also shown that the results of the FTIR measurements are highly dependent on the surface conditions, a small sanding study was performed to determine how sensitive the measurements might be to differences in sanding techniques [1, 2, 11]. For this study, the sanding variables that were investigated were the grit size, sanding method (hand versus orbital), and the sanding direction relative to the fiber. The difference between measuring on a ply and the more resin-rich layer between plies was already established; for this study, care was taken to sand the samples so that only 1 ply was exposed.

For the grit size study, three grit sizes (180 grit, 240 grit, and 320 grit) were chosen to give a variety of surface finishes with roughness that could be seen in a repair application. The direction of sanding was defined based on the orientation of the fiber. If the sanding was generally in the direction of the fibers, it was called parallel. Likewise, sanding that was more orthogonal to the fibers was called perpendicular. The sanding direction was defined from stereo microscope images. Example images for the different sanding directions are shown in figure 17. The brightness and contrast of the images were altered to make the sanding marks more visible.

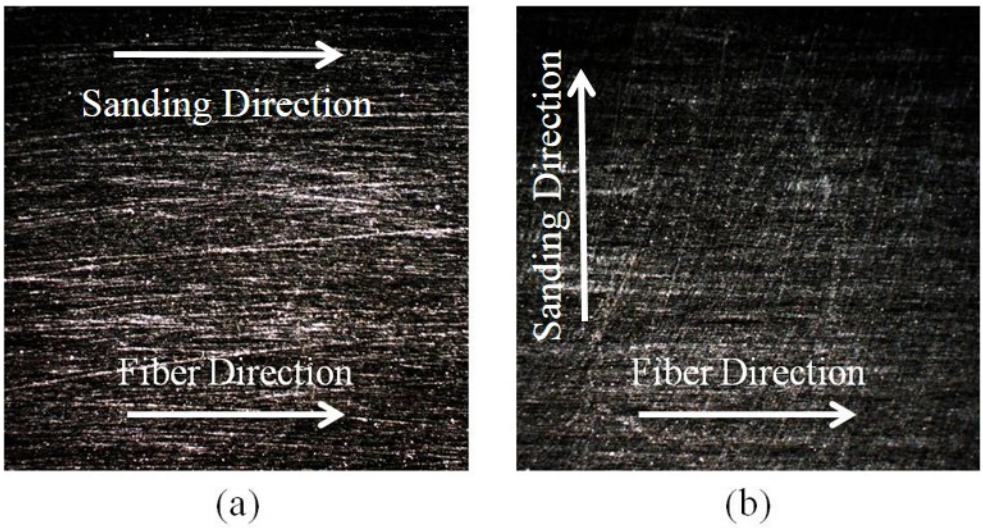

Figure 17. Stereo micrographs of sanded surfaces using orbital sander (a) parallel to fibers and (b) perpendicular to fibers

The sanding variables were evaluated using PCA, which is a statistical analysis method that transforms a dataset into a set of linearly uncorrelated variables called PCs. The first PC is transformed such that it contains the largest possible variance in the data. Each subsequent PC contains the next most variance possible under the constraint that it must be orthogonal to the preceding PCs [17]. Plotting PCs can be used to qualitatively identify similarities and differences between groups of samples. This is known as a scores plot. If data are clustered together and there is significant separation between the clusters, this indicates unique qualities within that sample set. PCA of the sanding variable studies was performed in GRAMS IQ software. Scores plots showing effects of the sample preparation variables are shown in figure 18. The ovals were added to indicate the boundaries of the clusters for each sanding factor.

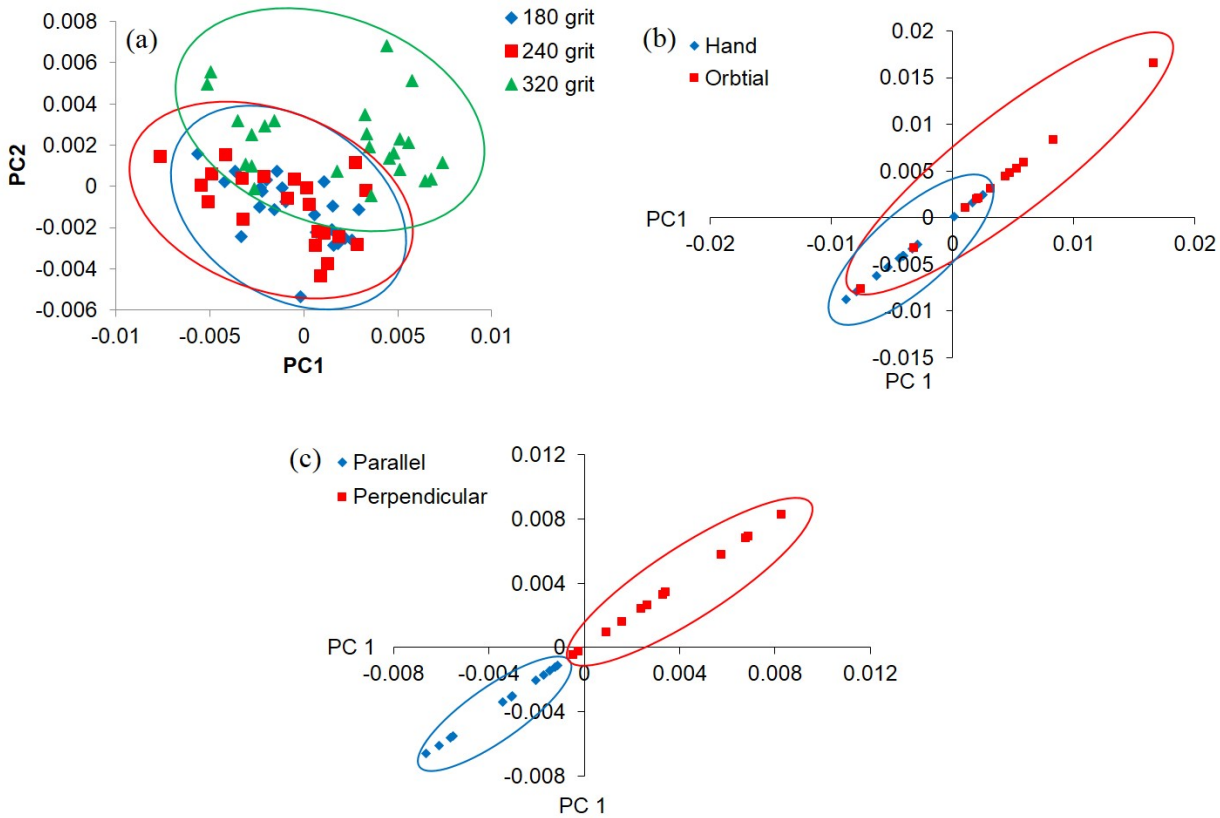

Figure 18. Scores plot for the sanding variables (a) grit size, (b) sanding method, and (c) direction relative to fiber

PCA analyzes all features in the data, whether or not they are related to the performance variable, making it a blind analysis technique. Larger differences in spectral features will result in more distinct clusters in the scores plots. Figure 18(a) shows that there is significant overlap between the clusters of the different grit sizes. This indicates that the PCA was not able to differentiate between the spectra of the samples sanded with the 180, 240, and 320 grit sizes used in this experiment. It is possible that more principle components are needed to differentiate the groups, that different pre-processing conditions may be needed to separate the differences, or that variation in the spectral features between the grit sizes was relatively small. Grit-size comparison charts show that the difference in average particle size between the grits was relatively small. The 180-grit sandpaper had an average particle size of ~76 µm, whereas the 320-grit sandpaper had an average particle size of 36 µm [18]. Therefore, it is likely that the changes in spectral features between the different grit sizes were relatively small. Because there were only two variables used in the sanding method and sanding direction studies, only one PC could be used for the scores plot. Therefore, these studies were plotted as PC1 versus PC1. For the sanding method study, overlapping clusters were observed, indicating that there was likely not a significant enough difference in the spectra of the samples for PCA to identify whether hand or orbital sanding was used. In contrast, the sanding direction scores plots exhibit separate and distinct clusters, signifying that sanding direction produced distinct differences in the spectra that could be discerned by PCA. As discussed in section 2.2.3.2, orientation of the FTIR relative to the fiber direction had a significant impact on the FTIR measurement, and it is likely that a

similar orientation effect is being observed with the sanding direction. Note that the magnitude of signal differences relative to the fiber direction is much smaller for the sanding direction than for the FTIR alignment. Though some of the conditions in this report are unlikely to occur in an actual repair (e.g., the sanding direction would be more random), this study is indicative of the importance of consistent sample preparation for analysis by FTIR. Therefore, it is critical to ensure that the surface finish of the part being inspected matches the finish of the calibration standards as closely as possible [1, 2, 11]. As a result, the SBS calibration samples and the panels inspected were all sanded using the same orbital sanders and sandpaper.

3.3.3 Model Development

Once a consistent level of sanding was achieved, FTIR measurements were taken on the calibration SBS set (the thermal exposures of that set are shown on the left side of table 1). As shown in figure 14, except for small differences in the baseline, it was difficult to distinguish the FTIR spectra on the fiber-rich surface with varying levels of thermal exposure. To eliminate baseline effects and accentuate differences, the spectra were processed using a Savitzky-Golay first derivative with seven smoothing points algorithm with mean-centering and multiplicative scatter correction. A plot of FTIR spectra after mean centering and taking the derivative is shown in figure 19.

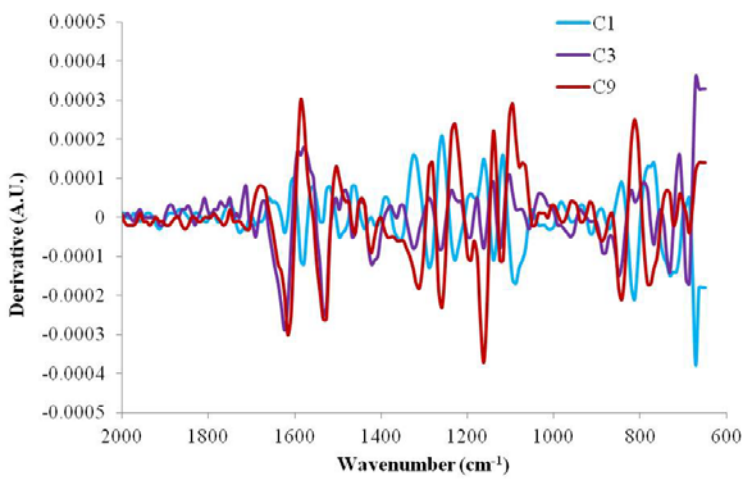

Figure 19. FTIR preprocessed with Savitzky-Golay first derivative and seven smoothing points

Although the differences are easier to see after taking the derivative, identifying trends in the data is still difficult and requires MVA. Using the results of the PCA in GRAMS IQ, a PLS model correlating the FTIR spectra to the F_{SBS} measurements was generated. The software used a leave-one-out cross-validation to optimize the PLS model by minimizing the root mean square error of cross-validation (RMSECV) [1]. The F_{SBS} data used for the model are shown on the left side of table 3 and were measured by the University of Delaware in Phase I of the project.

Table 3. F_{SBS} data for calibration and evaluation for BMS 8-276 SBS sets [11]

Sample group	F_{SBS} (MPa)	StDev	Rel. F_{SBS} [%]	Sample group	F_{SBS} [MPa]	StDev	Rel. F_{SBS} [%]
C1	84.4	1.4	95.1	E1	79.4	1.6	89.6
C2	76.5	2.9	86.2	E2	75.5	0.6	85.1
C3	72.0	3.6	81.1	E3	47.7	1.4	53.7
C4	80.7	3.3	90.9	E4	81.6	1.1	92.0
C5	74.5	0.9	84.0	E5	75.3	0.7	84.9
C6	43.9	0.9	49.5	E6	50.6	2.5	57.0
C7	83.0	1.6	93.5	E7	82.5	2.1	93.0
C8	76.0	3.2	85.6	E8	76.0	1.4	85.7
C9	52.0	0.8	58.6	E9	70.7	2.4	79.7
C10	82.1	2.5	92.5	E10	82.0	2.1	92.5
C11	79.3	1.7	89.4	E11	75.0	1.7	84.6
C12	61.8	3.1	69.7	E12	82.8	0.6	93.3
C13	81.9	2.6	92.3	E13	75.9	2.4	85.6
C14	73.5	1.4	82.9	E14	57.9	0.6	65.2
C15	82.8	2.9	93.3	E15	82.8	0.6	93.4
C16	79.1	0.7	89.2	E16	78.8	1.2	88.9
C17	55.9	1.6	63.0	E17	73.0	4.0	82.3
C18	83.5	3.8	94.2	E18	82.4	0.6	92.9
C19	76.2	5.4	85.9	E19	77.0	3.1	86.8
C20	72.8	1.1	82.0	E20	55.2	2.7	62.3

Several parameters were investigated to determine their effect on the model fit. Initially there were many parameters that were varied, including the pre-processing conditions, the number of PCs used for the model, and the frequency range of the FTIR spectra included in the analysis.

The first task was to determine good pre-processing conditions, including the smoothing algorithm and order of the derivative. The two smoothing algorithms in GRAMS IQ—Savitzky-Golay and GAP—were both investigated. Savitzky-Golay smoothing was found to produce better correlations than GAP for the calibration model. Varying the number of smoothing points from five to nine did not have much effect on the models. Similarly, the use of first-order derivatives was found to lead to better performance than the use of second-order derivatives. In contrast, second-order derivatives were used on the resin-rich surface calibration models developed in Phase I of the project [11].

The number of PCs used influences the robustness of a calibration model. Selecting too many PCs will incorporate noise into the model along with the variable of interest, causing increased prediction error (overfitting). Incorporating too few PCs can result in underfitting, which can increase the bias of predictions [19]. Choosing the correct number of PCs can be a complicated process. Initial attempts at determining the number of PCs for the model focused on minimizing

the standard error of cross-validation (SECV) while also inspecting the loading spectra of those PCs for signs of significant noise. The initial range of PCs investigated was from 3–6.

The frequency range is another important parameter because it determines which peaks are included in the analysis. It is possible to include peaks that vary between measurements but are not related to thermal exposure of the epoxy. An example of this is variations in ambient moisture causing changes in the water peak between measurements, which has no relevance to the damage state. PCA is a blind analysis that characterizes the largest variance in the data regardless of the source of the variation. Therefore, if there was a large variance in the measurements from something not related to ITD, it could affect the ability to obtain a good model. Initial modeling efforts focused on three main frequency regions: the full spectra from 4000–650 cm^{-1}, 3700–3000 cm^{-1}, and 2000–900 cm^{-1}. Neither end of the spectra was included in the frequency range because they contained large amounts of noise that resulted from instrument limitations rather than big changes in the signal.

The initial process was to restrict the frequency range and then select the number of PCs that minimized the RMSECV to find the best model. The best results were obtained using the peaks 2000–900 cm^{-1} range. Subsequent trials restricting frequencies in this range found that 1700–950 $^{cm-1}$ yielded good correlations. These results were similar to findings in other studies [1, 11]. According to the SECV versus the number of PCs plot provided by GRAMS IQ, it was found that five PCs minimized the SECV. Figure 20 shows a plot of the predicted F_{SBS} using the model with five PCs and a frequency range of 1700–950 cm^{-1} versus the actual measured F_{SBS} of the thermally exposed samples. The line represents the PLS regression.

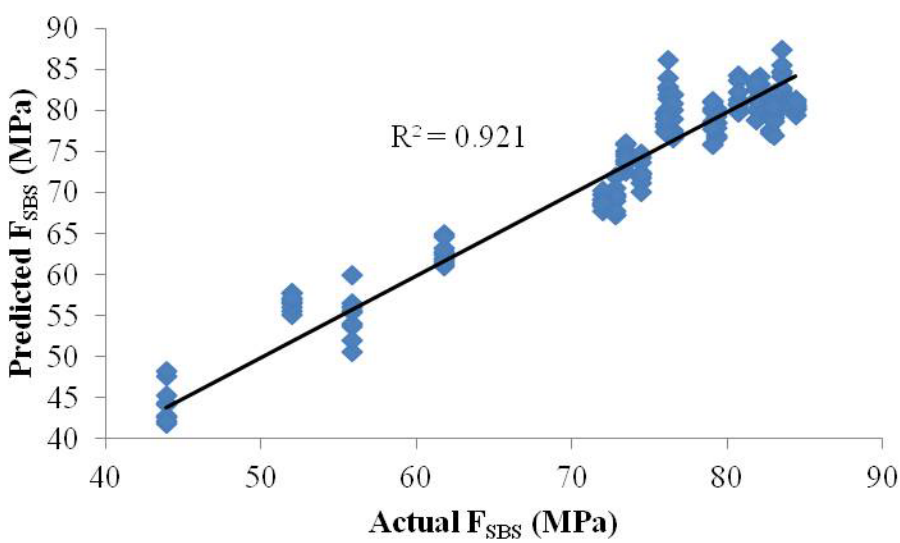

Figure 20. Predicted vs. actual F_{SBS} of a calibration set using a PLS regression with five PCs and a frequency range of 1700–950 cm^{-1}

The RMSECV for the calibration model with five PCs was 3.0 MPa, which was similar to that obtained for resin-rich surfaces in Phase I of this project [11]. To verify the accuracy of the calibration model, an independent evaluation SBS set was measured and predicted using the model made from the calibration set. The thermal exposures and F_{SBS} data for the evaluation set

is shown on the right side of tables 1 and 3, respectively. The predicted F_{SBS} versus the actual F_{SBS} for the evaluation set is shown in figure 21. The superimposed line represents the expected results if the predicted values matched the actual results.

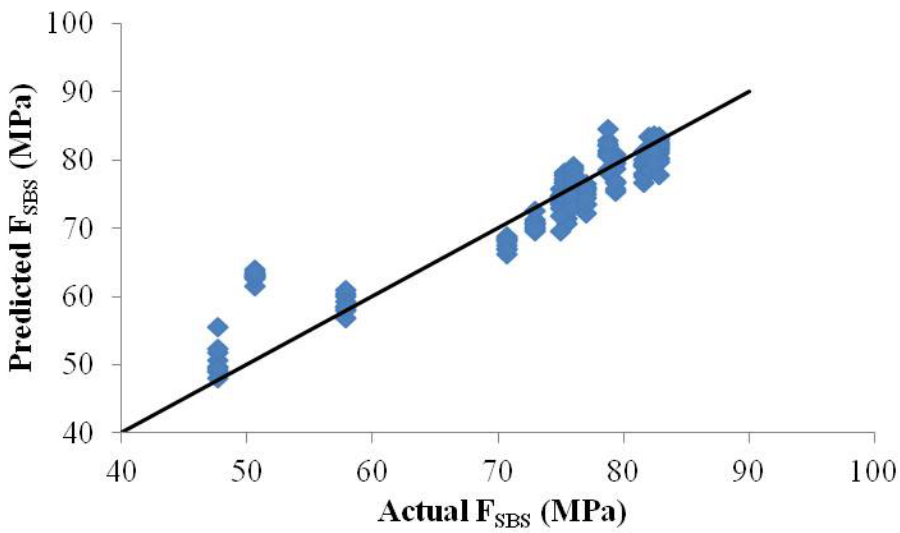

Figure 21. Predicted vs. actual F_{SBS} for the evaluation set

In figure 21, the majority of predicted values fall close to the line. The root mean square (RMS) error for the evaluation set was 4.2 MPa, which is higher than that for the cross-validation of the calibration set. Note that at F_{SBS} below 60 MPa, the predictions were almost always higher than the actual F_{SBS} value. This may be a result of the onset of delaminations, for which the F_{SBS} would no longer be a function of only the matrix thermal degradation. Delaminations were found in a similar composite system for comparable thermal exposures as the samples used for these experiments [2]. To evaluate the individual accuracy of the predictions, the relative error was calculated using equation 2:

$$\%\text{Error} = \frac{\text{predicted}-\text{actual}}{\text{actual}} * 100\% \tag{2}$$

The relative error was categorized into the following three categories for analysis based on the absolute value of the error: error less than 5%, error between 5%–10%, and error >10%. A histogram of the number of samples in each category from the prediction of the evaluation set is shown in figure 22.

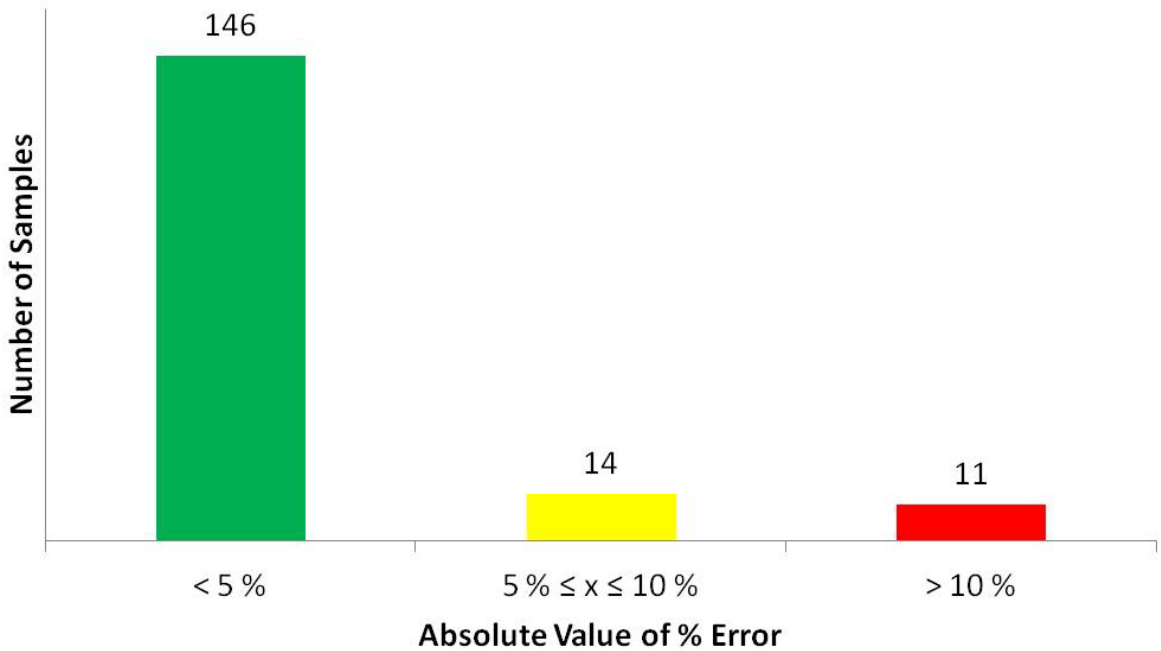

Figure 22. Histogram of relative error in prediction of evaluation set F_{SBS} from calibration model

Figure 22 shows that over 85% of the samples exhibited less than 5% error, indicating the model did an excellent job of predicting the F_{SBS} of the thermally damaged samples. The average error was 4.5%. Of the 11 predictions that had >10% error, nine came from the same set (E6) and all of them came from samples that were highly damaged (F_{SBS} <60 MPa). This may indicate that the model is less effective for predicting the remaining strength in highly damaged samples, which may be due to the onset of delaminations in the composite. PLS and chemometric MVA predict linear behavior. Once the SBS values change in nonlinear fashion, they would best be predicted in a go/no-go model instead of trying to predict the SBS values quantitatively.

3.3.4 Model Refinement

The calibration model developed in section 3.3.3 was used to do the initial mapping of the panels with localized damage and will be referred to as model 1. Early in the process of ply-by-ply mapping of the panels, it became apparent that model 1 required further optimization. Exposure maps were generated to visualize the impact from the localized heating of the panels. Each square in the heat map represented the predicted F_{SBS} values based on FTIR measurements at that grid point. Measurements were taken 1.3 cm apart from each other. On the colors scale, blue/green represents little to no ITD, and red indicates the most. Black squares indicate that either no measurement was taken in that area or that the location had been accidentally sanded through to the next ply. In other cases, measurements were disregarded when the spot was resin rich because this produced spectra that did not fit the calibration set of sanded panel spectra. Resin-rich areas on the surface plies were difficult to avoid during sanding from the tooled surface. As shown in figure 23, there is significant variation in the predictions by model 1 between plies. Many areas were predicted to exhibit higher levels of damage on the second ply

than on the first ply, when it was expected that damage would decrease further down into the composite. In figure 23, the number of columns was reduced for the second ply down because the predictions on the first ply down indicated that little to no damage remained in columns H and I. The go/no-go threshold for damage is discussed in section 3.4.2.

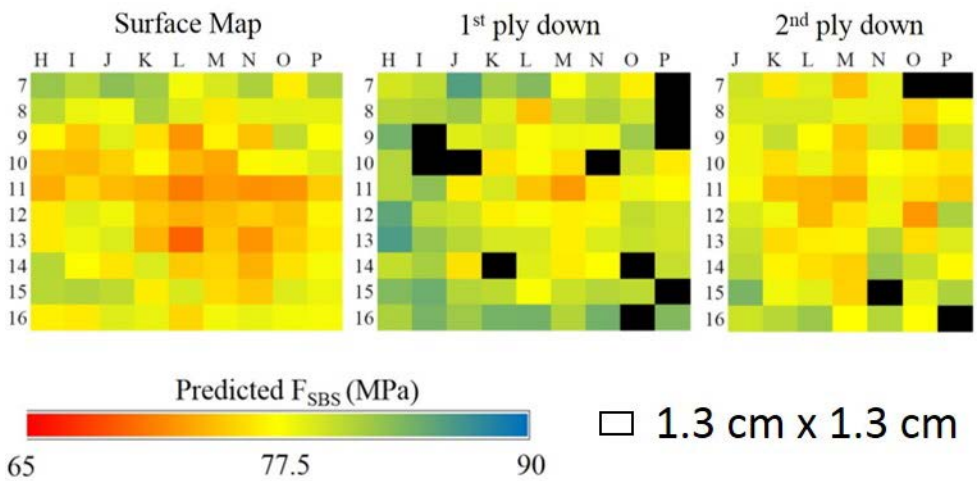

Figure 23. Model 1 prediction on medium-exposure panels

After examination of the spectra, it was determined that most of the error was likely due to the model and not the FTIR measurements. Model 1 appeared overly sensitive to slight variations in measurements. To determine if refining the model could mitigate the sensitivity issue, several of the key model parameters discussed in section 3.3.3 were investigated further. In addition to the number of PCs and the frequency range, the F_{SBS} values included in the set were also considered.

For the F_{SBS} values, it was observed that when the full set of calibration SBS values (ranging from ~43.9 MPa to 84.5 MPa) were used in the model, standards with F_{SBS} <60.0 MPa predicted higher than their actual SBS values. One possible cause for the model breaking down below 60.0 MPa is the onset of delaminations or other physical defects brought about at this level of thermal exposure. Structural damage could lower F_{SBS} without being detected by the FTIR measurements, which only measures chemical information of the matrix [2]. Damage, such as delamination, is outside the ITD regime and would be outside the scope of the FTIR inspection process. Fortunately, that level of damage would likely be found by other NDE methods, such as ultrasound. Including standards with lower F_{SBS} values due to structural weakening of the part in the calibration set could make the PLS model less accurate. Two cases were examined for the model refinement: models using all the SBS values in the calibration set and models using only datasets with F_{SBS} > 60.0 MPa.

As discussed in section 3.3.3, the number of PCs used could also influence the robustness of a calibration model. The high sensitivity to small changes in the spectra would suggest that model 1 may have been overfit, which could incorporate noise into the model that was not reproduced in measurements on the panel. The effects of incorporating 3–5 PCs to model this system were compared.

Another potential issue with model 1 is in the chosen frequency range. Specifically, variations in ambient moisture water peak at approximately 1645 cm^{-1} were observed, which had no relevance to the damage state. The SBS calibrations samples were stored in plastic containers, whereas the panels were stored in a box open to ambient conditions. Therefore, the panels were likely to have absorbed more water and potentially exhibited a greater variation in the water peak. To examine if the frequency range affected the model, two ranges were studied: 1700–950 cm^{-1} and 1600–950 cm^{-1}. The 1600–950 cm^{-1} range was chosen to eliminate variation in the spectra due to the water peak.

Table 4 shows a list of the models evaluated in this report. For brevity, the models presented are a subset of the variable combinations previously discussed. Though many models were examined, the following discussion demonstrates the path to optimization.

Table 4. PLS models and parameters

Model	F_{SBS} Values in Calibration Set	Number of Principal Components	Frequency Range (cm^{-1})
1	All	5	1700–950
2	All	3	1700–950
3	All	4	1700–950
4	$F_{SBS} > 60.0$ MPa	4	1700–950
5	$F_{SBS} > 60.0$ MPa	4	1600–950

As a first comparison, the different models were used to predict the independent evaluation set of SBS coupons described in section 3.3.3. Because several of the models did not incorporate samples with $F_{SBS} < 60.0$ MPa, all of the models were compared using only samples from the evaluation set with $F_{SBS} > 60.0$ MPa. The models were evaluated on three criteria: bias, RMS error, and the Mahalanobis distance (M-distance), which is a measure of how closely the measured spectrum matches the average calibration spectrum. A lower M-distance means a closer match between the measured and calibration spectra. The results of predicting the evaluation SBS set for each model are shown in table 5. The same set of spectra was used for each model prediction.

Table 5. Model predictions of SBS evaluation set

Model	Bias (MPa)	RMS Error (MPa)	Average M-distance
1	0.6	3.2	2.1
2	1.7	3.7	1.5
3	0.4	3.1	1.8
4	0.6	2.6	1.9
5	0.3	2.7	1.5

The bias in model 2 was considerably higher than the other models, which likely indicates that the model is underfit with three PCs [19]. Models constrained to using only samples with

F_{SBS} > 60.0 MPa exhibited lower RMS errors, indicating that the samples with lower F_{SBS} values affected the predictive capability of the models in the ITD range. This was likely caused by a combination of ITD and structural defects, such as delaminations, affecting mechanical strength. FTIR can only measure chemical changes in the resin related to ITD. Model 1 had the highest average M-distance and a higher RMS error, which may be a result of noise incorporated into the model by overfitting. From the evaluation set predictions, the models with four factors performed the best overall when evaluating all three criteria.

The models were also evaluated on their predictions for the surface and first and second plies down on the medium-exposure panel, where shortcomings of model 1 first became apparent. One of the issues was that the M-distances for spectra taken on sample panels were noticeably larger than from predicting the evaluation set of SBS coupons. The average M-distances varied depending on the models, but were typically >3 and often >5 when using spectra measured on the panels. Although M-distance is only one measure of data quality, large M-distances may indicate that a given spectra is significantly different than the calibration spectra and, therefore, can reduce the confidence in the ability of the model to predict the value of the spectra accurately. Some possible explanations for high M-distances are differences between the panels and the SBS coupons in the sanding and/or in moisture content. FTIR measurements have been shown to be sensitive to sanding (resin richness, sanding pattern, and surface finish) of the part. To achieve low M-distances, the sample being measured needs to have a surface finish as close as possible to the calibration set [1, 2]. However, because of the differences in the sample size, it was difficult to achieve consistent sanding on the surface between the calibration SBS sets and the larger panels. This difference may be mitigated by producing the model from larger calibration coupons. Another possible cause of this issue could be differences in the water content between the calibration set and the sample panels. There was a difference in the storage of the SBS samples and the panels that could have created a difference in moisture content between the samples. For the panel predictions, model 5, which excluded the water peak at 1650 cm^{-1}, typically exhibited the lowest M-distance values.

A comparison of predicted F_{SBS} values is shown in figure 24. The same FTIR spectra were used to generate the ply maps for each model. Only the portion of the surface ply that was considered damaged using model 1 is presented here. Model 3 was excluded to conserve space as the variation was greatest between the models shown.

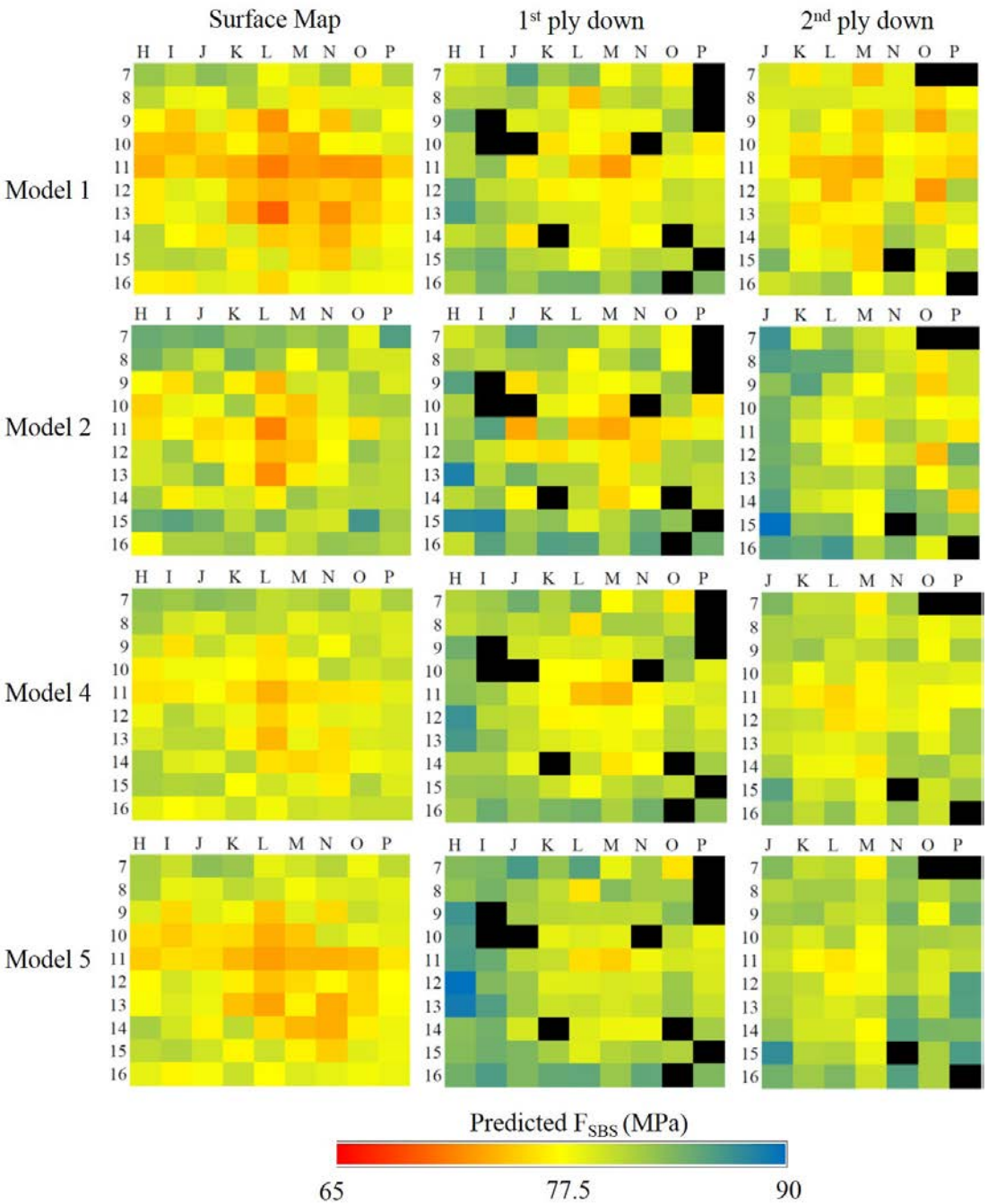

Figure 24. Comparison of model predictions for medium-exposure panel for (left) surface ply, (middle) 1st ply down, and (right) 2nd ply down

The surface ply maps in figure 24 show that all of the models predict the highest damage near the center of panel, as would be expected. However, model 1 predicts that the significant damage (orange) spreads farther than in the other models. There is also a small difference between the value of the highest damage (lowest F_{SBS}) predictions between the models that used all the SBS samples and the models constrained to $F_{SBS} > 60.0$ MPa. Models 1 and 2 tended to predict higher thermal exposure than models 4 and 5. The prediction of the levels of ITD in the panel in

models 4 and 5 were closer to the expected damage based on the similar thermal exposures in the calibration and evaluation sets.

The biggest difference between the models occurred when going from the first subsurface ply to the second ply down. Model 1 actually predicted a noticeable decrease in F_{SBS} (increased ITD), especially in columns K and M. The issue with model 1 is likely a result of overfitting, in which noise that does not significantly affect the other models created instability of the predictions. Model 2 also exhibits some instability, such as in column J on the first and second ply down, where areas jump from damaged (orange) to little damage (blue-green). Columns H and I were not measured in the second ply down because they were considered to have little to no damage after the first ply down. The go/no-go threshold for damage is discussed in section 3.4.2.

The differences between models 4 and 5 were small, but both models had difficulties, given certain spectral features. Model 5 generally predicted much lower F_{SBS} values than model 4 when the spectra was taken from a resin-rich location, as described in section 3.3.1. Resin-rich locations tended to predict low in most of the models. Model 4 was more sensitive to changes in the water peak at 1645 cm^{-1}. Spectra with high levels of noise typically produced higher F_{SBS} predictions. Most of the blue squares were the result of noisy spectra.

Models 4 and 5 were similar in their predictions in the absence of noise and differences in moisture. However, because they excelled at handling different spectral interferences, both models were used to evaluate the panels. The surface ply, which was often resin rich because it was sanded from a tooled surface, was predicted using model 4 because it was less sensitive to the resin-rich spectra. Model 5 was chosen to complete the mapping of subsurface plies because the wavenumber range excluded visibly noisy areas and water peaks in the spectra.

3.4 PANEL MAPPING RESULTS

3.4.1 Surface Mapping of Panels

In Phase I of the project, surface maps were made on the resin-rich tooled surface of the panels with localized damage by Boeing and A_2 Technologies [11]. This initial surface mapping was used to get an idea of how well the damage predictions on the fiber-rich sanded surface compared to determine the effectiveness of the model predictions. The methodology and color scaling for the damage on the resin-rich surface were not explicitly detailed in the report so a direct comparison could not be made, but the general shape, location, and relative level of damage could be compared. In the mapping on the resin-rich surface, dark blue represents the least damage, and red and brown areas represent the most damage. The scale for the mapping on the fiber-rich sanded surface is provided. Figure 25 shows both sets of maps.

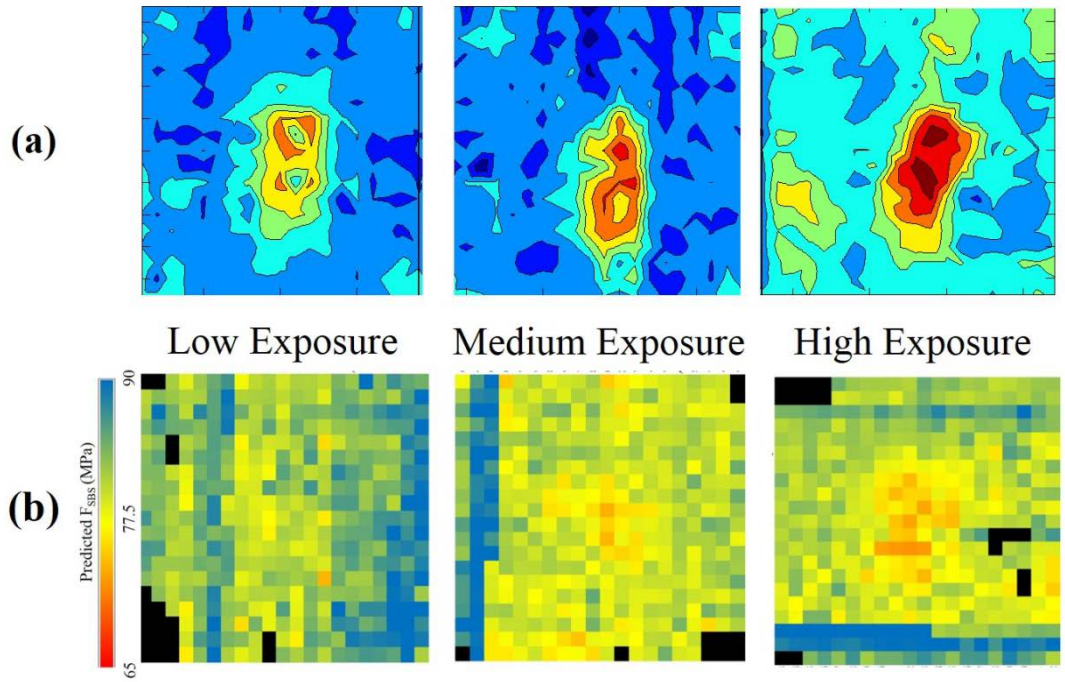

Figure 25. Surface maps made on (a) a resin-rich tooled surface and (b) a fiber-rich sanded surface predicted with model 4 (note that scales, panel orientation, and color schemes are different between (a) and (b))

Figure 25 shows that the relative location, shape, and damage match relatively well between the resin-rich and fiber-rich sanded surface predictions. This reinforced that the predictions on the sanded surfaces were working well. Note the elongated shape of the damage in the panels, which is likely a result of thermal exposure on unidirectional panels as a result of better heat conduction in the fiber direction than perpendicular to it. Features of individual surface maps will be discussed in sections 3.4.2–3.4.4.

3.4.2 Low-Exposure Panel Mapping

The purpose of this research was to investigate how well the FTIR could identify ITD so that it could be removed during the repair process. One of the issues that arises when performing such a task is determining when the damage can be considered removed and the panel ready for repair. The initial plan was to take FTIR measurements on a sample with no thermal exposure to determine what F_{SBS} value the model would predict for a sample with no damage. The model predicted an F_{SBS} value of 84.7 ± 1.9 MPa for the undamaged specimen with a low of approximately 80 MPa. According to the SBS testing, an undamaged specimen would have an F_{SBS} of approximately 88.8 MPa. The predictions were lower than expected. In addition, the average M-distance was >9, indicating the spectra was not a good match with the calibration set. The high M-distances were likely caused by not including a sample without thermal exposure in the calibration model. Though the model prediction seems reasonable, the high M-distance makes it difficult to trust these values. Instead, the criterion for determining the end point of the inspection was determined by examining the low-exposure panel, which was expected to have minimal ITD based on comparable thermal exposures of the calibration set. Though the

low-exposure panel may not have required repair, the center region was sanded down two plies to assess the scarf-and-measure process to determine where predicted F_{SBS} values level out or fall below a go/no-go threshold. The ply mapping of the low-exposure panel is shown in figure 26.

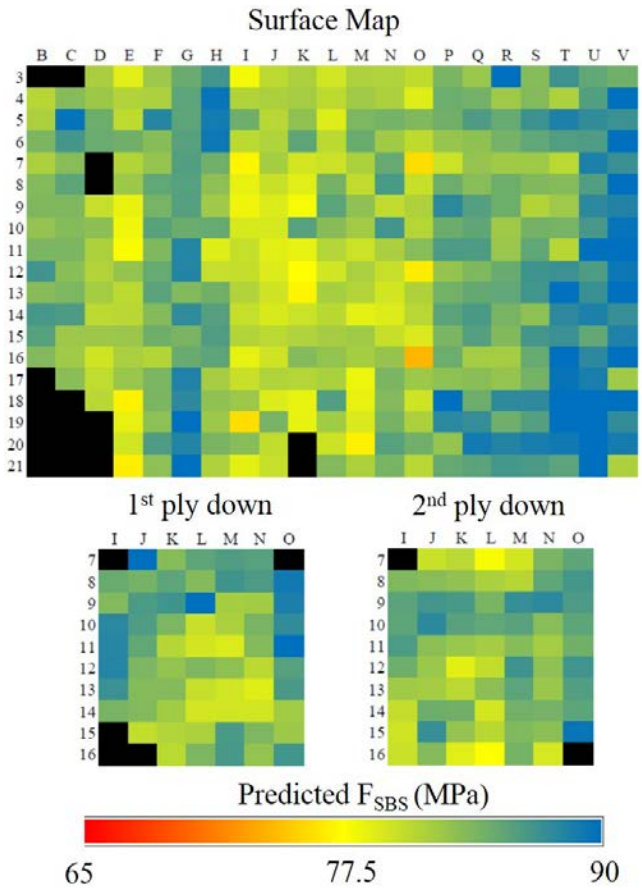

Figure 26. Ply-by-ply map of predicted damage on a low-exposure panel; the surface map was predicted using model 4 and subsurface plies were predicted using model 5

Figure 26 shows that the highest ITD on the surface ply map, except for one location, was yellow (77.5 MPa), indicating that there was minor ITD. This value was close to F_{SBS} of C8 (76.0 MPa) from table 3, the closest thermal exposure in the calibration set. A small percentage of the spots predicted an F_{SBS} less than 75 MPa (orange colored), but these were found to have resin-rich spectra and were not likely related to damage sites. The strong blue-colored area was found to have been caused by spectra with high noise levels.

Sanding down one ply in the center raised all the F_{SBS} values in the area above 79 MPa. Although some decrease in F_{SBS} was predicted between the first and second ply down, no value dropped below 78 MPa. The changes in values were within the expected errors of the model. The standard deviation of the difference between measurements on the first and second plies down was ~2.7 MPa. The standard deviation for predictions from measurements at the same location on a single ply was ~0.9 MPa. The differences between the variation between the plies and the variation when taking measurements at one location may be attributed to several variables, including surface finish (reflectivity), resin content, moisture content, and distance from the heat

source. In addition, there is potential alignment error because the rulers used for alignment were manually placed. The variation between the first and second plies down was similar to the RMS error of the evaluation set and, therefore, appears to be a reasonable measure of the variation between plies.

The areas outside of the damaged area were considered when setting the go/no-go threshold. By taking the average of the values outside of the damage and accounting for the variation in the measurements, it was decided that F_{SBS} >79.5 MPa could be considered the threshold value, especially when such a value was observed in the same location on more than 1 ply. This corresponds to an F_{SBS} retention of ≥90%. In the heat maps, this condition appears as a medium-green to blue square. Using this condition, the low-exposure panel would be considered clear of any damage after the first ply down.

3.4.3 Medium-Exposure Panel Mapping

The full mapping of the medium-exposure panel is shown in figure 27.

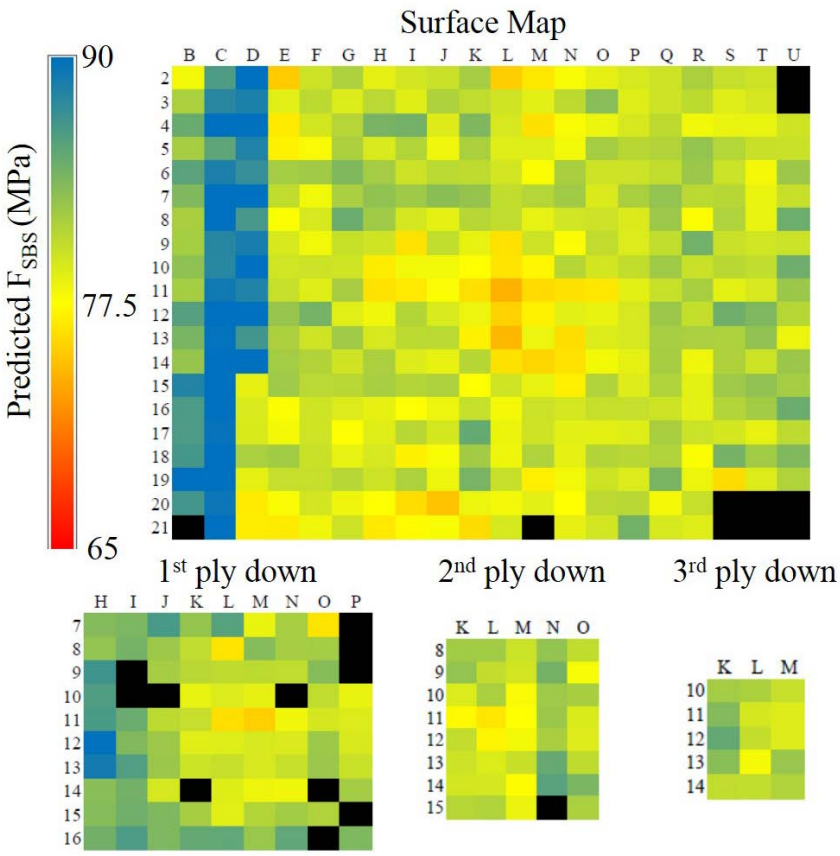

Figure 27. Ply-by-ply map of predicted damage on medium-exposure panel: the surface map was predicted using model 4 and sub-surface plies were predicted using model 5

The surface ply map in figure 27 shows that the medium-exposure panel had ITD in the center region approximately 7.6 cm x 7.6 cm. This was expected because that was the location of the hot spot. The lowest predicted F_{SBS} values were approximately 74–75 MPa. The magnitude of the

predicted damage was comparable to set C5 (74.5 MPa), which was the closest thermal exposure from the calibration set. The orange boxes outside of the center were ignored because they were found to be caused by resin-rich areas and were likely not indicative of thermal damage. The grid area from H7–P16 was chosen as the boundary of the damage area to be removed by sanding. After sanding to expose the first subsurface ply, only L11 and M11 were predicting F_{SBS} values of less than 76 MPa, with other areas of light damage (yellow-green) around the area. F_{SBS} for the second subsurface ply increased slightly in the previously damaged area, and only a small area in columns L and M remained below the acceptance criterion of 79.5 MPa; however, the damage prediction was within RMS error for the model of the acceptance criteria. After reaching the third ply down, all the locations except for L13 were above the acceptance criterion, and L13 was only slightly below 79 MPa. Therefore, after sanding down 3 plies on the medium-exposure panel, the damage was considered removed. There were a few locations on the third ply down where the panel had been sanded through to the next ply down. To improve the bonding surface for the repair, the medium-exposure panel was sanded down an additional ply in the same region as the third ply down. This ply was not mapped because of time limitations, and the damage was considered removed at this point.

3.4.4 High-Exposure Panel Mapping

The mapping of the high-exposure panel is shown in figure 28.

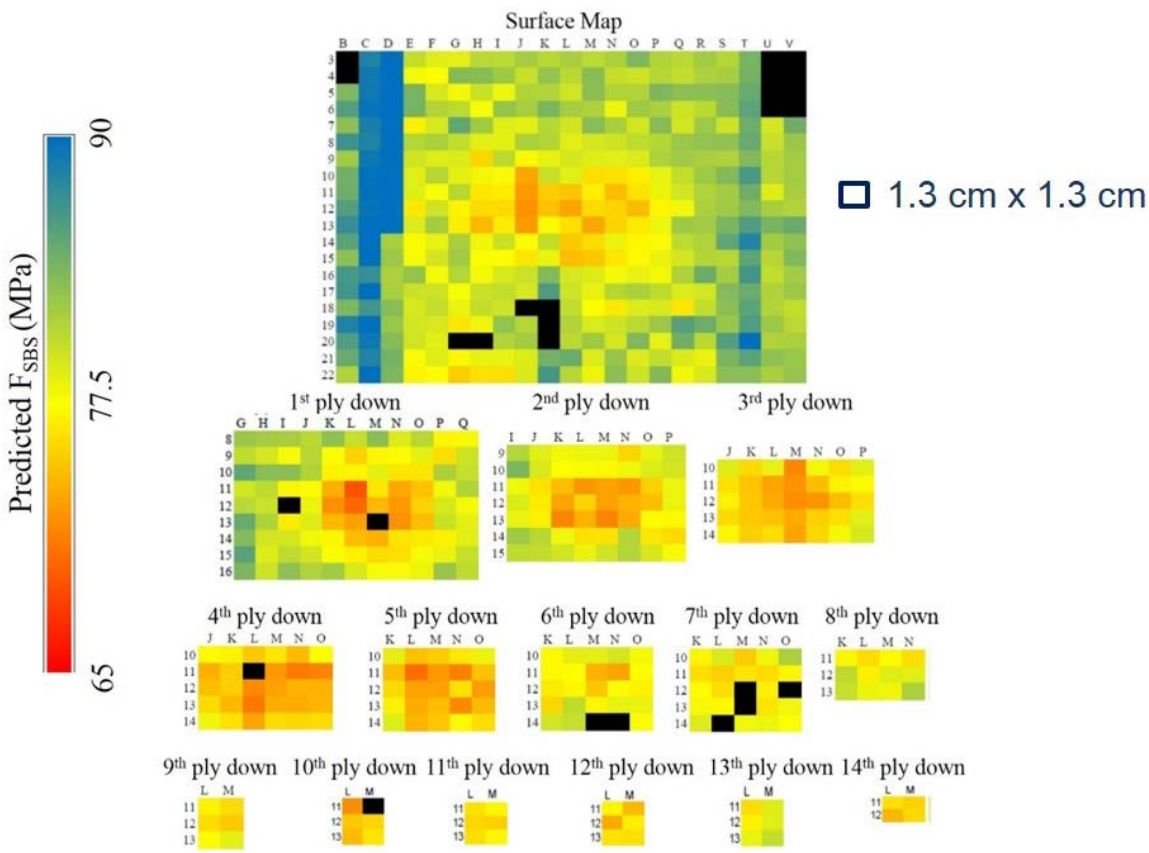

Figure 28. Ply-by-ply map of predicted damage on a high-exposure panel: the surface map was predicted using model 4, and subsurface plies were predicted using model 5

The surface ply mapping of the high-exposure panel showed more ITD over a larger area (G8–Q16) than the panels exposed to lower temperatures. This corresponded to an approximately 12.7 cm x 12.7 cm area. The lowest F_{SBS} values predicted on the surface were approximately 72–73 MPa. The calibration set had no thermal exposure that was close to the high-exposure panel, but C3 and E9 did have values of 72.0 MPa and 70.7 MPa, respectively. The trend of a gradual increase in F_{SBS} value was observed for the first 2 plies down, similar to that in the medium exposure case. However, on the third and fourth plies down, the predicted F_{SBS} decreased in many areas. It is unclear why this change in behavior occurred. No clear differences or trends were observed between spectra from the third and fourth plies down and the preceding plies. Note that the third and fourth plies down had an average M-distance of 5.4 and 5.0, respectively, which was higher than most of the plies measured, which typically varied from ~3.0–3.8. However, on the fifth ply down, the predicted F_{SBS} values were comparable to the third ply down, but the average M-distance on the fifth ply down was 3.6. The predicted F_{SBS} began to increase again on the sixth ply down through the eighth ply down. The panel was sanded to expose the 14th subsurface ply in the region of L11–M12, but the predictions became erratic, often predicting lower than the previous ply. This may have been an issue with obtaining consistent sanded surfaces in such a small area deep in the composite. Therefore, there was less confidence in the predictions after the ninth ply down. Improving the match of the surface finish between the calibration standards and sample to be measured may help mitigate these issues. In any case, the predicted F_{SBS} values below the ninth ply did not approach the acceptance criteria. There is a distinct possibility that damage existed that far into the composite because a backside temperature of 420°F was measured during the thermal exposure of the panel.

Inspection was stopped after the 14th ply because of limitations to the size of the repair. To perform a scarf repair, a certain scarf angle must be maintained, and the farther down into the panel the repair area, the bigger the scarf repair becomes. After sanding down 14 plies, the required repair size was approaching the size of the panel, so the inspection process had to be stopped if a repair was to be performed (see figure 7(c)).

3.5 TENSILE TESTING OF PANELS

During the panel inspection with the FTIR, it was difficult to determine how good the predictions were because there was no reference set of data to compare the F_{SBS} predictions to, as in the case of the measurements on the SBS samples. Therefore, to determine the quality of the inspection, it was decided to perform mechanical testing on the repaired panels to determine if the damage was successfully removed. As discussed in section 2.1.2, the original plan was to have another set of panels with the low, medium, and high exposures that were not repaired to compare to the strength of the repaired panels. However, after cutting up the panels for testing, it was found that the damaged panels had a quasi-isotropic stacking sequence instead of the unidirectional stacking of the repaired panels. Therefore, it was not possible to compare the two sets of panels. A unidirectional panel with localized thermal damage was fabricated at UW as a test panel prior to this discovery to verify that the tensile testing would be sensitive to the damage. That panel was exposed at 480°F for 1 hour, which falls between the medium- and high-exposure panels. Because of time limitations, this was the only available panel to mechanically test for thermal damage. In addition to the thermally damaged panel, two control panels were also fabricated: one

pristine, undamaged panel and a control panel with no damage but a large repaired area to account for any changes to the strength as a result of the repair.

The average 45° tensile strength for each of the panels is shown in figure 29. The error bars represent one standard deviation. Though seven samples were tested for most of the panels, several samples from each panel failed in the grips and were not included in the average strength calculations. Many of the samples that failed in the grips failed at strengths consistent with the set being tested, but they were excluded because failure in the grip is undesirable during testing. Therefore, the average strengths are calculated from 3–6 samples for a given panel. Stress-strain plots for all the samples from each panel are provided in appendix A.

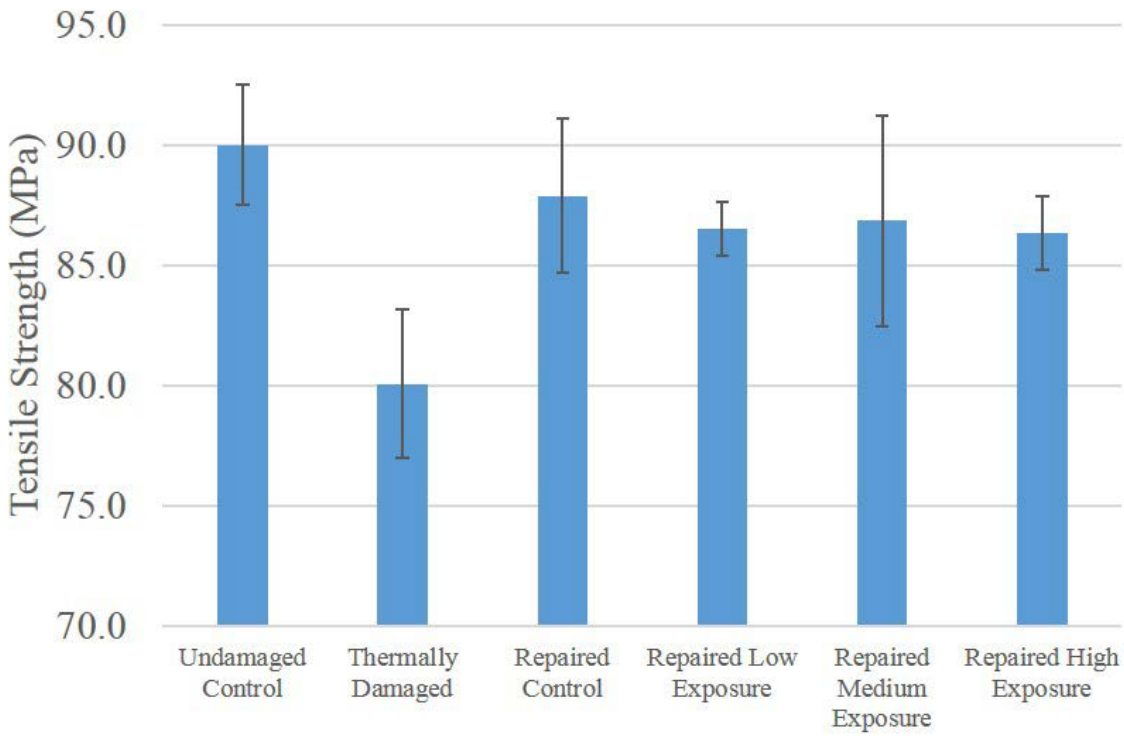

Figure 29. The 45° tensile test results

Figure 29 shows that the undamaged control panel had the highest 45° tensile strength (approximately 90 MPa). The three repaired panels had a similar strength to the repaired control panel, with strengths ranging from 86–88 MPa. As expected, the strength of the repaired panels was less than that of the undamaged panels because the fibers were not continuous through the repair patch, though the difference between repaired panels and the undamaged panel was not statistically significant, according to a student t-test with a 95% confidence interval. The thermally damaged panel had the lowest strength of the panels at 80 MPa. Because of the gradient of thermal exposure, the strength varied away from the center of exposure. The two samples at the center of the exposure were weaker and had strengths of 76.3 and 79.6 MPa. A student t-test with a 95 % confidence interval revealed that the differences between the damaged panel and the other panels were statistically significant. Considering the repaired panels all had similar strengths and were significantly higher than the damaged panel, it is reasonable to

conclude that most of the damage was removed from the panels inspected with the FTIR. The repaired high-exposure panel may still have had some residual damage; the inspection process was not completed because of repair size limitations (see section 3.4.4). If damage was present on the high-exposure panel, it had little impact on the strength measurements. Without more testing, it is not possible to determine if excess undamaged composite was removed during the inspection process. However, initial results indicate that the FTIR guided repair was successful at removing ITD from the panels.

The failure mode for all the samples was the same, but the failure location in a given sample often varied. According to the classification for failure in ASTM D3039, all samples exhibited an angled failure mode with approximately a 45° angle [15]. This failure mode was expected for a unidirectional panel being pulled at 45° from the fiber orientation. The samples from the center of the thermally damaged panels (TD3–TD5) failed at the center, near the region where the highest thermal exposure occurred. No other discernable pattern was observed for the location of failure in any of the other panels. Many of the repaired samples failed near the center, but many also failed close to the grips, and a few failed in the grips. Images of the failed samples from the thermally damaged panel and the repaired high-exposure panel are shown in figure 30. The images of all the tensile specimens after failure are in appendix A.

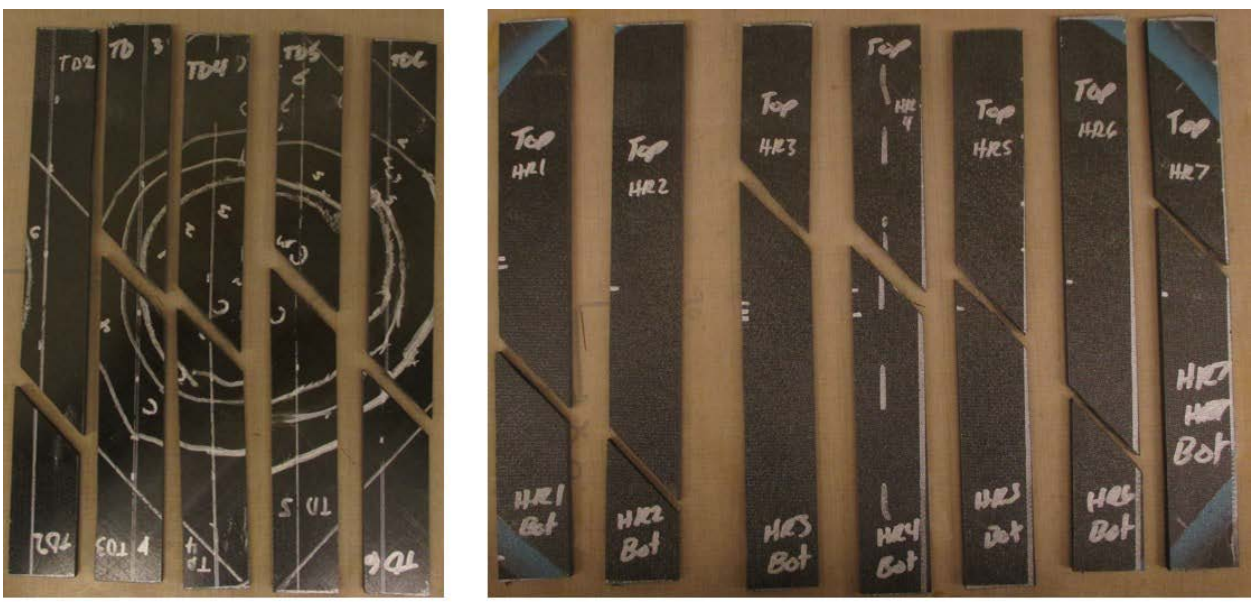

(a) (b)

Figure 30. Failed tensile samples of (a) a thermally damaged panel and (b) a repaired high-exposure panel

4. SUMMARY OF RESULTS

4.1 FLUORESCENCE MEASUREMENTS

Fluorescence intensity was observed to decrease with increased exposure time when measured on the resin-rich tooled surface; however, the intensity measurements were difficult to repeat and

were not recommended for evaluating ITD. The λ_{max} of the fluorescence peak was also observed to redshift with increased exposure time/temperature. However, the shifts did not monotonically correlate to SBS measurements. It may be possible that the shifts correlate to a different mechanical property, but only F_{SBS} data were available for this study. No fluorescence was measured on fiber-rich sanded surfaces, which may be attributed to many factors, including a decrease in signal due to a decrease in resin content, fluorescence caused by oxidation products removed during sanding, or another excitation wavelength needed to excite fluorescence on the sample.

4.2 CA MEASUREMENTS

No discernable correlation between CA measurements and F_{SBS} measurements was observed on the resin-rich tooled surface or the fiber-rich sanded surface with increased exposure time/temperature for either DI H_2O or DIM. The only trend that was observed was that the fiber-rich surface exhibited lower CA measurements than the resin-rich surface. Therefore, CA initial results suggest CA measurements are not suitable for inspecting for ITD.

4.3 FTIR

Phase II of this project focused on investigating the use of the handheld Exoscan FTIR for guiding repairs of panels with localized ITD. In Phase I of the project, a PLS model that successfully correlated FTIR measurements to F_{SBS} measurements on resin-rich surfaces was generated. However, it was discovered that the fiber-rich surface of a sanded composite exhibited a significantly different FTIR spectra, partly due to the removal of the oxidation peak from the spectra after sanding. Therefore, a new model had to be developed to use the FTIR to guide repair on a sanded composite. The model was developed by systematically investigating many different variables that could affect the model. The variables that were investigated were sanding variables, preprocessing conditions, and varying the frequency range used in the model and the number of PCs incorporated into the model.

For the sanding variables, in the range of sizes studied, it was found that grit size did not have a significant effect on the measurements. It was also not possible to differentiate hand sanding from orbital sanding. However, it was possible to differentiate whether the sanding was parallel or perpendicular to the sanding direction. This confirmed a point made in previous reports that the surface preparation of the samples to be inspected needs to be as close as possible to the surface preparation of the calibration samples to achieve the best results.

Trying to obtain a correlation between the raw FTIR spectra to F_{SBS} measurements was difficult because there was little difference in the spectra for a low and high thermal exposure on the fiber-rich sanded surface. To accentuate differences between the spectra, preprocessing parameters were investigated. It was found that the Savitzky-Golay first derivative with seven smoothing points yielded the best results. Because of the scattering of the IR light on the rough surface and carbon fibers, multiplicative scatter correction was also applied during pre-processing.

To obtain a good model to correlate the FTIR spectra to F_{SBS} data, two primary model parameters were investigated: the number of PCs incorporated into the model and the frequency range. The

number of PCs controls whether the model has a good fit or if it underfits or overfits the data. The frequency range controls that peak in the spectra are included in the model. After trying many different combinations of these two parameters, a model was found that had predictive capabilities comparable to the model for the resin-rich surface from Phase I of the project. The first model generated had five PCs and was focused on the region of 1700–950 cm^{-1}. The predictive capabilities of the model were validated by using the model to predict F_{SBS} for an independently measured SBS evaluation set. The error in the model predictions of the evaluation set were on par with the prediction errors from Phase I of the project. This model was called model 1.

After using model 1 for surface mapping and a ply-by-ply inspection for panels with localized ITD, it was found that the model F_{SBS} predictions were erratic. Sometimes the model would predict much higher than expected (less damage), and other times it would predict lower than expected (more damage). A more focused study of the model parameters, specifically the number of PCs and the frequency range, was performed to see if the model performance could be improved. Additionally, the effect on limiting the calibration set to F_{SBS} values >60 MPa on performance was investigated.

It was observed that model 1 had a tendency to predict samples with values less than 60 MPa at higher than the actual values, possibly because of the addition of structural defects into the highly damaged samples that the FTIR measurements could not account for. It was found that model 1 may have been overfit with five PCs and, therefore, likely incorporated noise into the model that made the predictions erratic. It was determined that the best fit came from four PCs. Limiting the frequency range to 1600–950 cm^{-1} appeared to give a small improvement in the performance, possibly from the exclusion of a water peak at 1650 cm^{-1} that could cause variability in the signal. Lastly, it was found that limiting the calibration set to samples with F_{SBS} >60 MPa also gave a slight improvement in performance. Limiting the sample set in this way was deemed acceptable; if structural damage was occurring, then the damage was beyond the ITD range and would likely be detectable by ultrasound. The new models were compared to the results from the initial ply-by-ply inspection from model 1 and the new models, models 4 and 5, were found to be more stable than model 1. The new models also predicted closer to the expected values for the initial damage on the panels based on the thermal exposure levels.

The inspection process was continued using the new models. The low-exposure panel was found to have little damage and was used to establish a go/no-go threshold for determining when damage was sufficiently removed. The threshold was set at a prediction of 90% F_{SBS} retention for this study based on the measurements in and around the thermally exposed area. The medium-exposure panel was found to have a larger initial damage area than the low-exposure panel. Using the go/no-go threshold, it was determined that damage was removed after sanding down 3 plies on the medium-exposure panel. The high-exposure panel exhibited the largest damage area, as expected. Some instability in the measurements was observed on the high-exposure panel, which suddenly predicted more damage between the third and fourth plies down. However, the predictions somewhat stabilized until after 9 plies down, where the predictions became less stable again. The later instability may have been caused by difficulties achieving consistent sanding surfaces deep in the panel. After measuring down 14 plies on the

high-exposure panel, the model was still predicting locations that were below the go/no-go threshold; however, the inspection had to be stopped because of limitations related to the size of the repair.

After finishing the inspections, the inspected panels were all repaired using a scarfed repair process. Ultrasound measurements did not show any significant defects in the repairs. To determine if the damage had been removed from the panels, tensile testing was performed on the repaired panels along with an undamaged control panel, a repaired control panel, and a panel with a localized thermal exposure of 480°F for 1 hour. No statistically significant difference was found between the strength of the repaired panels and the strength of the undamaged or repaired control. The lower strength of the thermally damaged panel compared to all of the other panels tested was found to be statistically significant with a 95% confidence interval. Based on these results, it was concluded that most, if not all, of the damage in the panels inspected with FTIR was removed. It was not possible to determine if the inspection process had removed a significant portion of undamaged material in the panels (i.e., predict that good material was damaged).

Based on the results of this study, the handheld Exoscan FTIR is capable of guiding a repair process to remove ITD. However, to improve the reliability and performance for the ITD detection, more work needs to be completed to understand such issues as how to design surface preparation on calibration samples to closely resemble surface prep on in-service parts for inspection, as well as studying how different spectral artifacts can affect the model predictions. In addition, more work to refine the model parameters could potentially improve the predictive capabilities of the process.

5. REFERENCES

1. Shelley, P.H., Vahey, P., Werner G.J., and Seelenbinder, J., "Handheld Infrared Spectroscopy for Composite Non-Destructive Testing," *SAMPE Technical Conf*erence *Proceedings*, Long Beach, California, May 23–26, 2011.

2. Olshenske, Z., Milan, W., and Meilunas, R.J., "Overview of NAVAIR NDI Programs for Composite Heat Damage Assessment," *SAMPE Conference Proceedings: New Materials and Processes for a New Economy*, Seattle, Washington, May 17–20, 2010.

3. Fischer, W.G., Storey, J.M.E., Sharp, S.L., Janke, C.J., and Wachter, E.A., "Nondestructive Inspection of Graphite-Epoxy Composites Heat Damage Using Laser-Induced Fluorescence," *Applied Spectroscopy*, Vol. 49, No. 9, 1995, pp. 1225–1231.

4. Farquharson, S., Bassilakis, R., DiTaranto, et al., "Measurement of Thermal Degradation in Epoxy Composites by FT-Raman Spectroscopy," *Proceedings of SPIE* 2072, February 7, 1994, pp. 319–331.

5. Dara, I., Ankara, A, Akovali, G., and Suzer, S., "Heat-Damage Assessment of Carbon-Fiber-Reinforced Polymer Composites by Diffuse Reflectance Infrared Spectroscopy," *Journal of Applied Polymer Science*, Vol. 96, No. 4, May 15, 2005, pp. 1222–1230.

6. Street, K.N., Russell, A.J., and Bonsang, F., "Thermal Damage Effects on Delamination Toughness of a Graphite/Epoxy Composite," *Composite Science and Technology*, Vol. 32, No. 1, 1988, pp. 1–14.

7. Sathish, S., Welter, J., Reibel, R., and Buynak, C., "Thermo-Elastic Characterization of Heat Damage in Carbon Fiber Epoxy Composites," *Review of Progress in Quantitative Nondestructive Evaluation*, Vol. 25, 2006, pp. 1015–1019.

8. Brady, S.K., Conradi, M.S., and Vaccaro, C.M., "NMR Detection of Thermal Damage in Carbon Fiber Reinforced Epoxy Resins," *Journal of Magnetic Resonance*, Vol. 172, No. 2, February 2005, pp. 342–245.

9. Howie, T., Shi, Z., Jang. S.H., et al., "Detection of Thermal Damage of CFRP Using Fluorescent Thermal Damage Probe," *Proceedings of 44th International SAMPE Technical Conference*, Charleston, South Carolina, October 22–25, 2012.

10. Howie, T., Shi, Z., Jang. S.H., et al., "Time-Temperature Indicator for Evaluating Incipient Thermal Damage of CFRP," *SAMPE Technical Conference Proceedings*, Seattle, Washington, June 2–5, 2014.

11. Rein, A., "Advanced Fourier Transform Infrared Spectroscopy for Analyzing Damage in Aircraft Composites," FAA Report DOT/FAA/TC-14/26, October, 2014.

12. Boerio, F.J., Roby, B., Dillingham, R.G., Bossi, R.H., and Crane, R.L., "Effect of Grit Blasting on the Surface Energy and Composition on Graphite/Epoxy Composites," *Proceedings of 37 ISTC*. Seattle, Washington, October 31–November 3, 2005.

13. Chamberlain, J.R. and Robertshaw, V.L., "Wettability of Swellable Nonwovens: Determination of Contact Angle Against Swellable Nonwoven Material," *Application Lab*, Kruss USA, 2004.

14. "Standard Test Method for Short-Beam Strength of Polymer Matrix Composite Materials and Their Laminates," ASTM D2344-00, ASTM International, 2006.

15. "Standard Test Method for Tensile Properties of Polymer Matrix Composites," ASTM D3039, ASTM International, 2014.

16. Buch, X. and Shanahan, M.E.R., "Influence of the Gaseous Environment on the Thermal Degradation of a Structural Epoxy Adhesive," *Journal of Applied Polymer Science*, Vol. 76, No. 7, May 2000, pp. 987–992.

17. Abdi, H. and Williams, L.J., "Principal Component Analysis," *Wiley Interdisciplinary Reviews: Computational Statistics*, Vol. 2, No. 4, July/August 2010, pp. 433–459.

18. "Sandpaper," available at http://sizes.com/tools/sandpaper.htm.

19. Gowen, A.A., Downey, G., Esquerre, C., and O'Donnel, C.P., "Preventing Over-Fitting in PLS Calibration Models of Near-Infrared (NIR) Spectroscopy Data Using Regression Coefficients," *Journal of Chemometrics,* Vol. 25, No. 7, July 2011, pp. 375–381.

APPENDIX A—TENSILE TEST RESULTS

The stress-strain curves for each sample from the tensile testing are presented in this appendix. On the plots, the solid lines represent samples with acceptable failure modes, and the dashed lines indicate samples that failed in the grips and were excluded from the average tensile strength calculations.

A.1 UNDAMAGED PANEL

The stress-strain curves for the undamaged panel are shown in figure A-1.

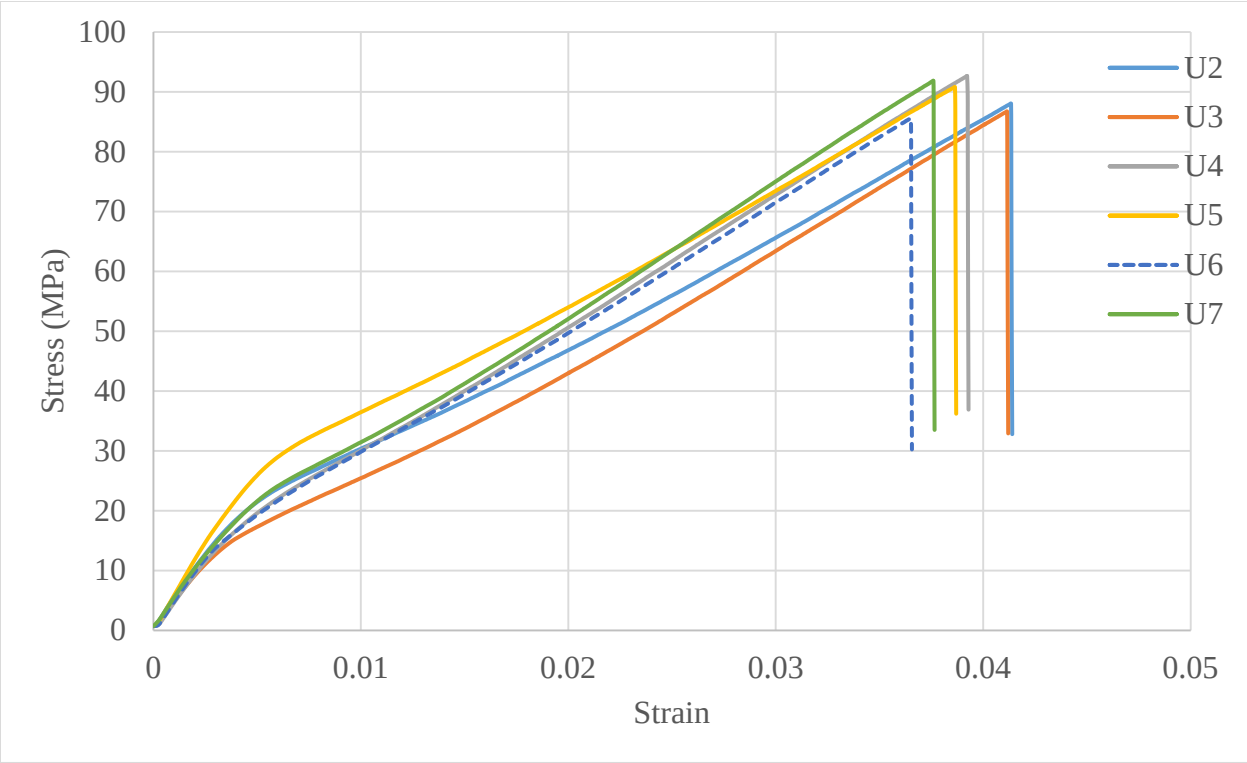

Figure A-1. Tensile test stress-strain curves for undamaged control panel

Images of the failed undamaged control panel are shown in figure A-2. The location of the failure in the undamaged samples typically occurred near the grips. Sample U6 was the only sample that failed in the grips.

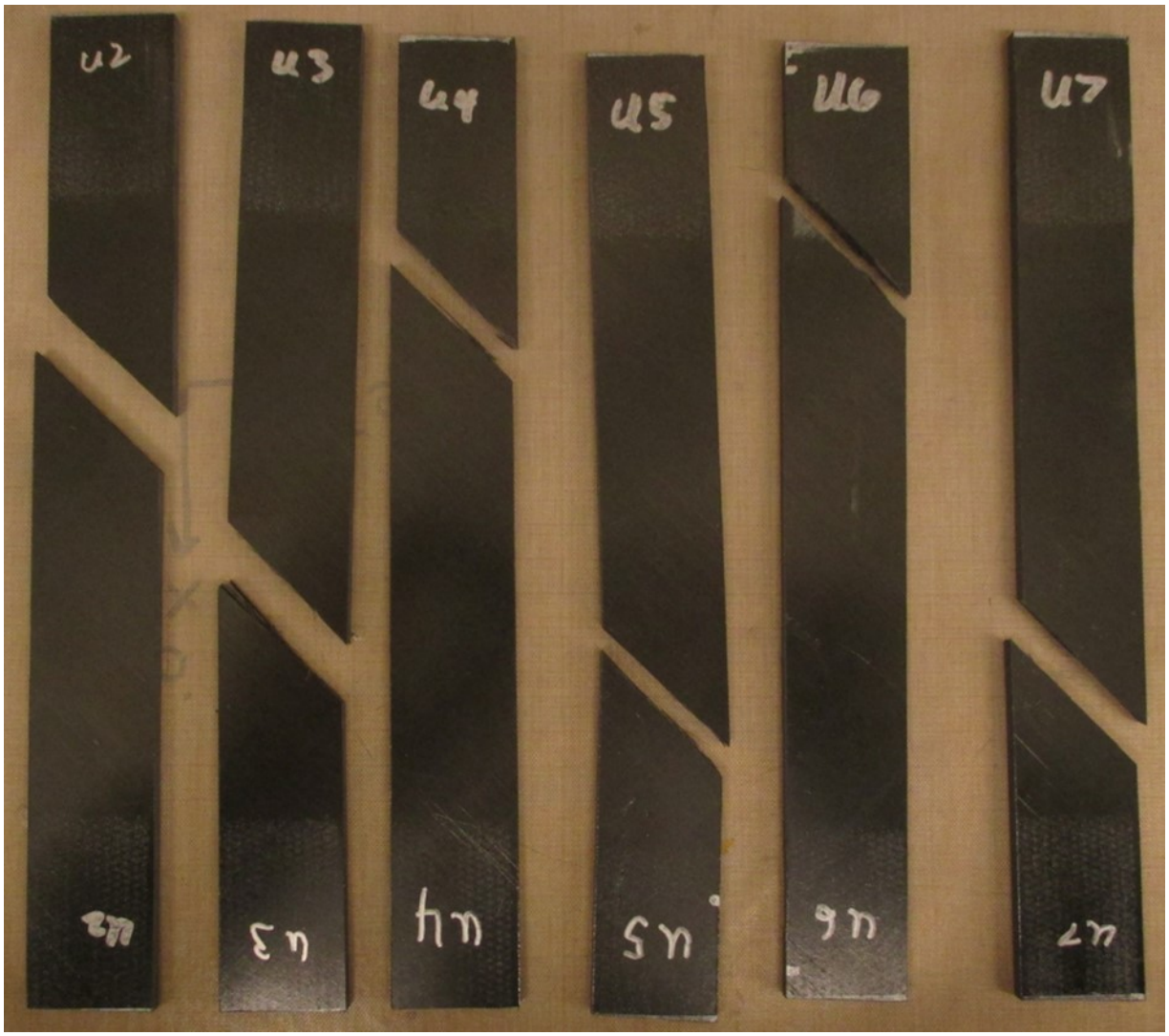

Figure A-2. Undamaged control panel tensile samples after testing

A.2 REPAIRED CONTROL PANEL

The stress-strain curves for the repaired control panel are shown in figure A-3. The gage length of the repaired control panels was mistakenly not measured prior to testing, so the lengths used to calculate strains were based on estimates from measurements after testing.

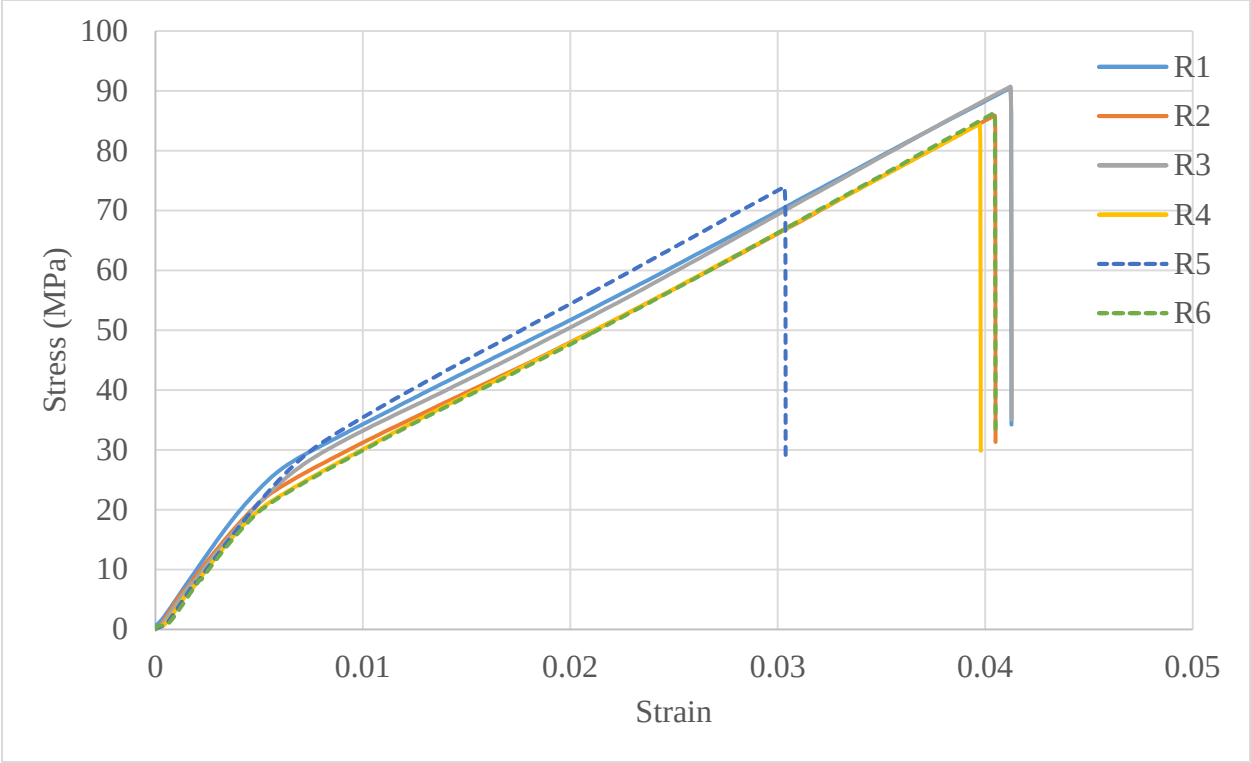

Figure A-3. Tensile test stress-strain curves for repaired control panel

A picture of the failed repaired control samples is shown in figure A-4. Samples R1–R4 failed in the center of the repair area. Both R5 and R6 failed in the grips.

Figure A-4. Repaired control panel tensile samples after testing

A.3 THERMALLY DAMAGED PANEL

The stress-strain curves for the thermally damaged panel are shown in figure A-5.

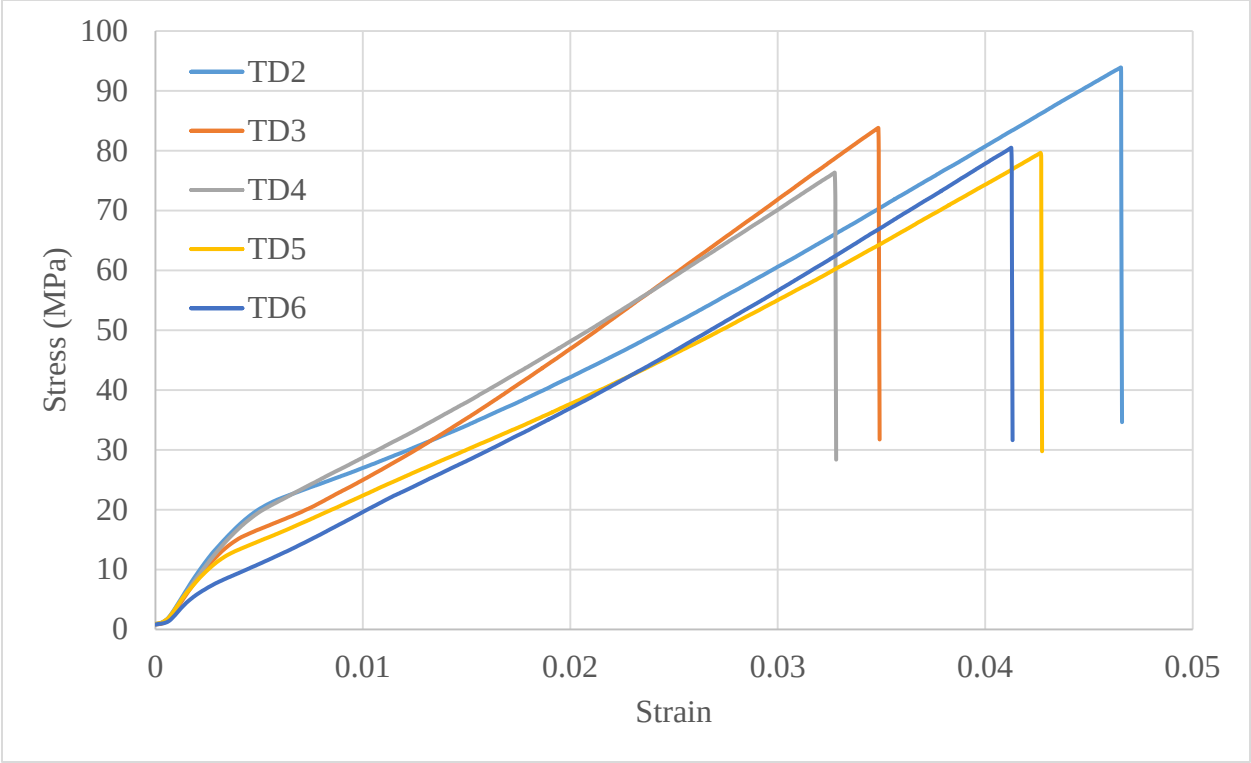

Figure A-5. Tensile test stress-strain curves for thermally damaged panel

The failed samples for the thermally damaged panel are shown in figure A-6. The TD3, TD4, and TD5 samples failed in the center of the sample near the area of highest thermal exposure. Sample TD2 was outside the main exposure area and failed near the grip.

Figure A-6. Thermally damaged panel tensile samples after testing

A.4 REPAIRED LOW-EXPOSURE PANEL

The stress-strain curves for the repaired low-exposure panel are shown in figure A-7.

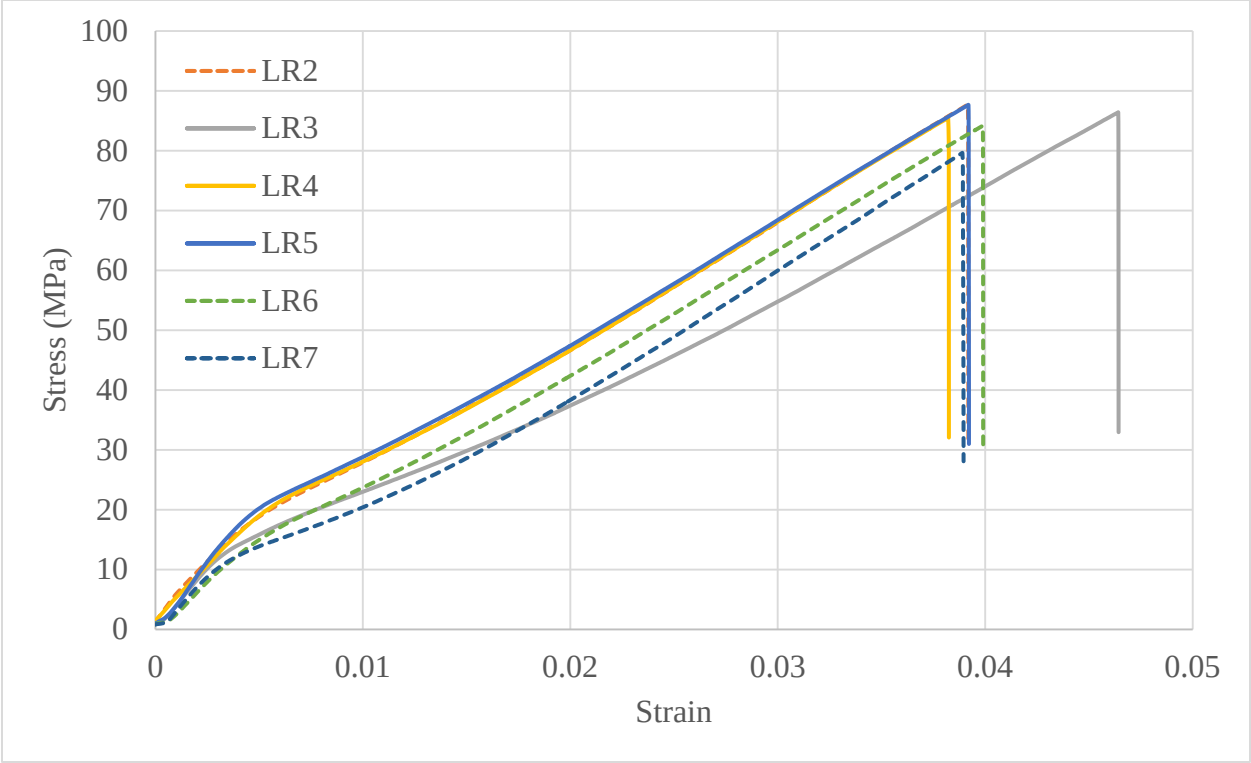

Figure A-7. Tensile test stress-strain curves for repaired low-exposure panel

The failed samples for the thermally damaged panel are shown in figure A-8. Samples L3, L4, and L5 failed in the repaired area near the center of the sample. Samples L2 and L6 failed in the grips. Sample L7 failed near the grips at the edge of the repair and exhibited lower strength than the other samples. It is possible that the porosity seen in the ultrasound in figure 8 of the main report near the edge of the repair may have been responsible for the reduced strength.

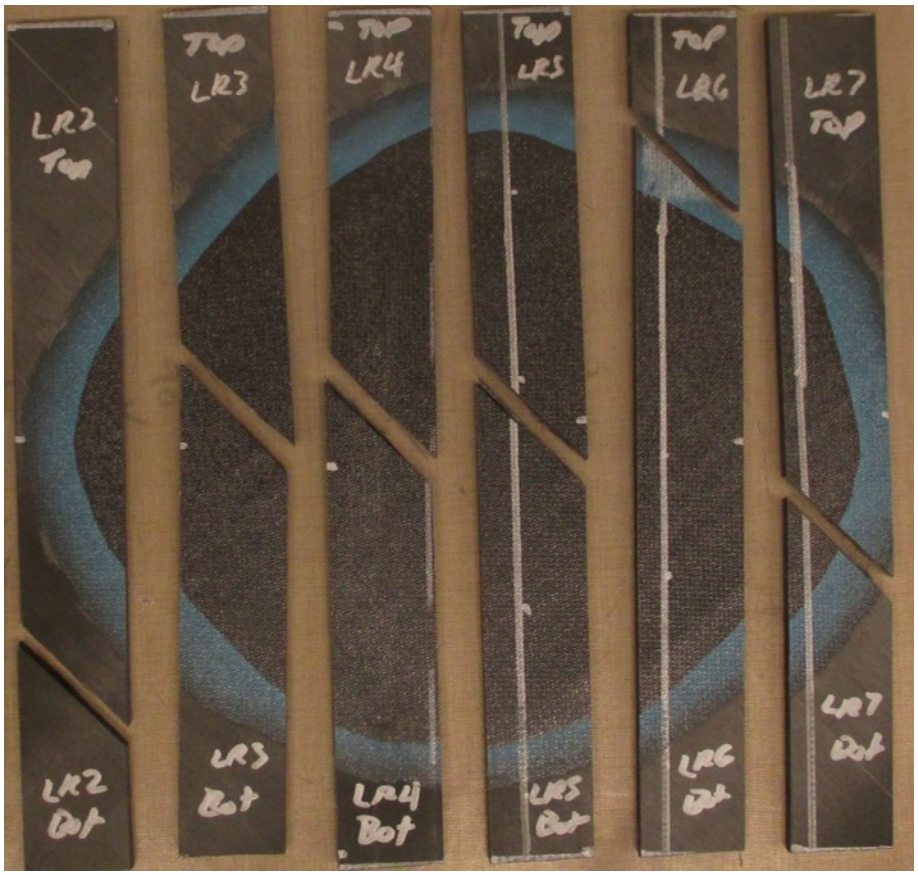

Figure A-8. Repaired low-exposure panel tensile samples after testing

A.5 REPAIRED MEDIUM-EXPOSURE PANEL

The stress-strain curves for the repaired medium-exposure panel are shown in figure A-9.

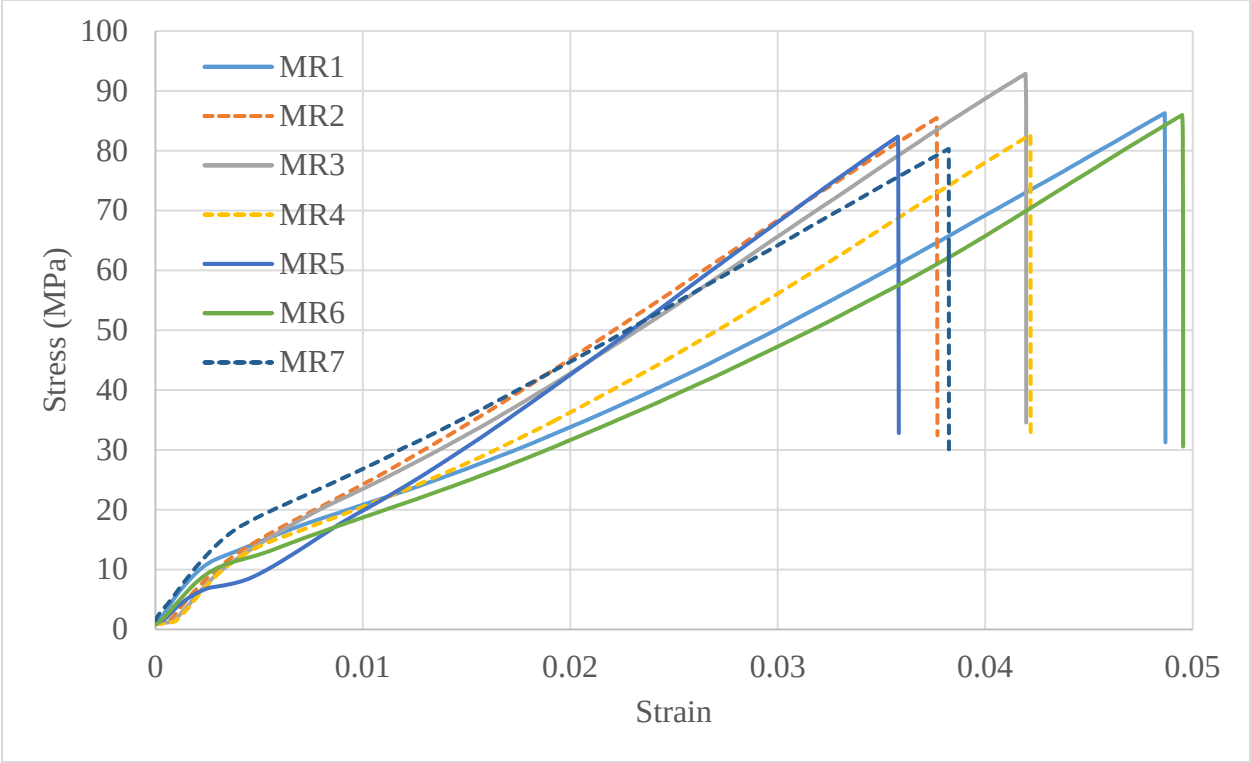

Figure A-9. Tensile test stress-strain curves for repaired medium-exposure panel

The failed samples for the repaired medium-exposure panel are shown in figure A-10. Samples MR2, MR4, and MR7 failed in the grips. Samples MR1, MR3, and MR6 failed near the grips. Sample MR5 was the only sample to fail close to the center.

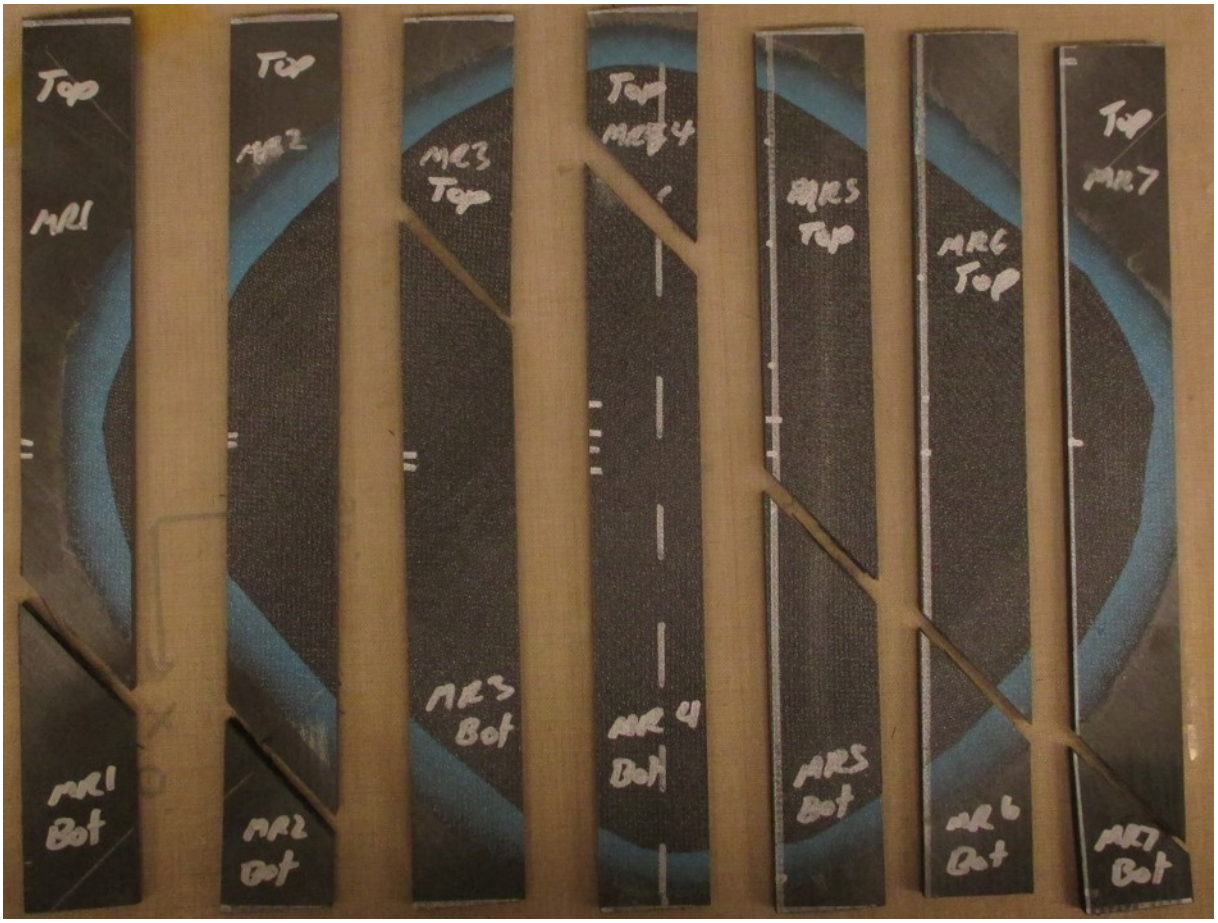

Figure A-10. Repaired medium-exposure panel tensile samples after testing

A.6 REPAIRED HIGH-EXPOSURE PANEL

The stress-strain curves for the repaired high-exposure panel are shown in figure A-11.

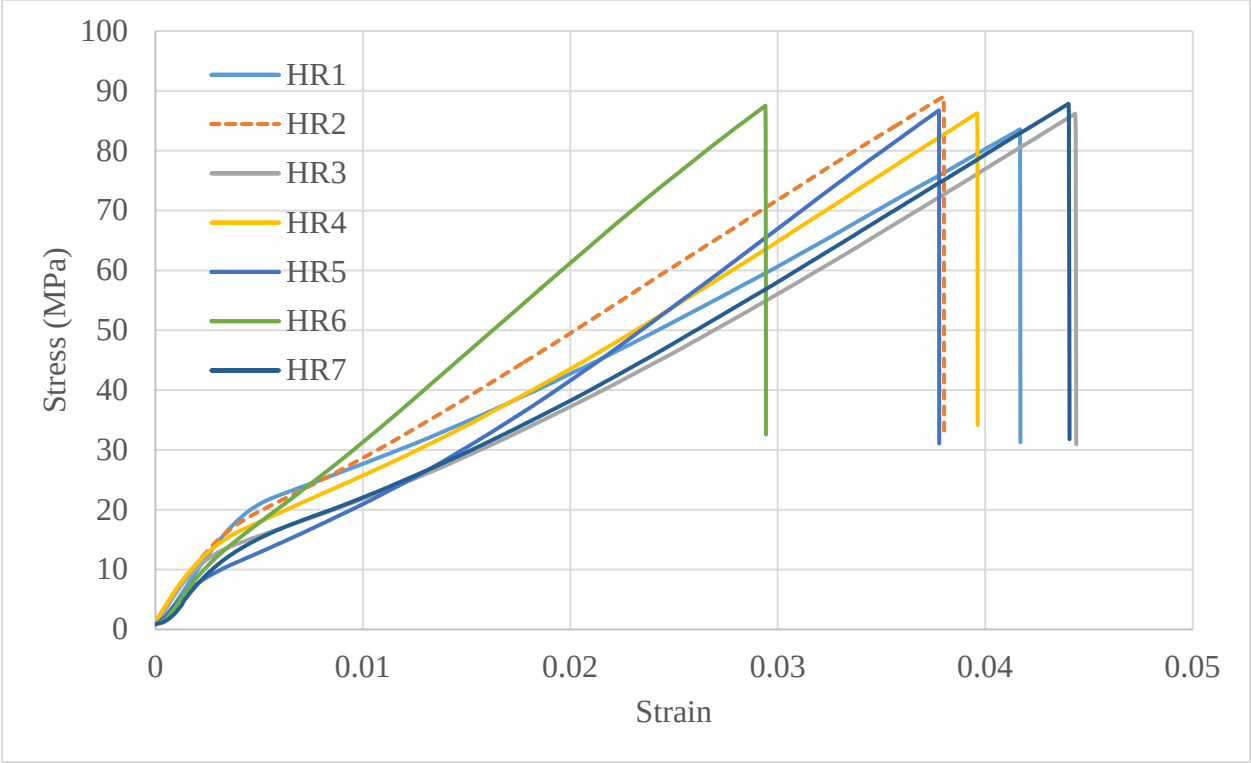

Figure A-11. Tensile test stress-strain curves for repaired high-exposure panel

The failed samples for the repaired high-exposure panel are shown in figure A-12. Only sample HR2 failed in the grips. Samples HR4 and HR5 failed near the center of the sample, whereas all of the other samples failed near the grips.

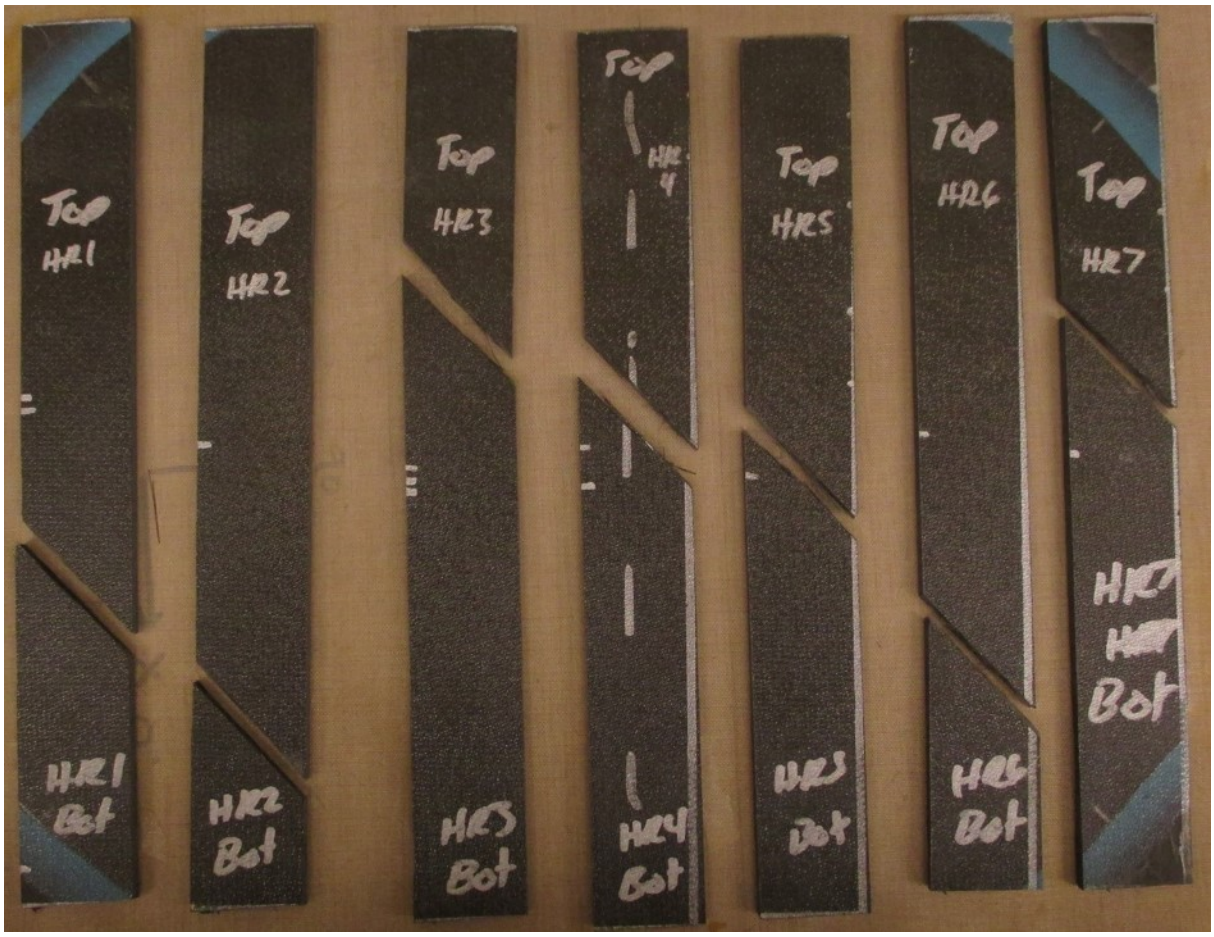

Figure A-12. Repaired high-exposure panel tensile samples after testing